JGR Atmospheres

RESEARCH ARTICLE
10.1029/2023JD040332

Constraining Present-Day Anthropogenic Total Iron Emissions Using Model and Observations

Sagar D. Rathod[1,2], Douglas S. Hamilton[3], Lance Nino[1,4], Sonia M. Kreidenweis[1], Qijing Bian[1], Natalie M. Mahowald[5], Andres Alastuey[6], Xavier Querol[6], Adina Paytan[7], Paulo Artaxo[8], Barak Herut[9], Cassandra Gaston[10], Joseph Prospero[10], Shankararaman Chellam[11], Christoph Hueglin[12], Daniela Varrica[13], Gaetano Dongarra[13], David D. Cohen[14], Patricia Smichowski[15], Dario Gomez[15], Fabrice Lambert[16], Francisco Barraza[17], Gilles Bergametti[18], Sergio Rodríguez[19,20], Yenny Gonzalez-Ramos[19,21], Jenny Hand[22], Katriina Kyllönen[23], Hannele Hakola[23], Patrick Chuang[24], Philip K. Hopke[25], Roy M. Harrison[26], Randall V. Martin[27], Brenna Walsh[27], Crystal Weagle[27], Willy Maenhaut[28], Yasser Morera-Gómez[29], Yu-Cheng Chen[30], Jeffrey R. Pierce[1], and Tami C. Bond[31]

[1]Department of Atmospheric Science, Colorado State University, Fort Collins, CO, USA, [2]La Follette School of Public Affairs, University of Wisconsin-Madison, Madison, WI, USA, [3]Marine, Earth and Atmospheric Sciences, North Carolina State University, Raleigh, NC, USA, [4]Columbia University, New York, NY, USA, [5]Department of Earth and Atmospheric Sciences, Cornell University, Ithaca, NY, USA, [6]Institute of Environmental Assessment and Water Research (IDAEA-CSIC), Barcelona, Spain, [7]Institute of Marine Sciences, University of California, Santa Cruz, CA, USA, [8]Instituto de Fisica, Universidade de Sao Paulo, Sao Paulo, Brazil, [9]Israel Oceanographic & Limnological Research, Haifa, Israel, [10]Rosenstiel School of Marine and Atmospheric Science, University of Miami, Miami, FL, USA, [11]Department of Civil & Environmental Engineering, Texas A&M University, College Station, TX, USA, [12]Swiss Federal Laboratories for Materials Science and Technology (EMPA), Duebendorf, Switzerland, [13]Dip. Scienze della Terra e del Mare, University of Palermo, Palermo, Italy, [14]Australian Nuclear Science and Technology Organization, Lucas Heights, NSW, Australia, [15]Comisión Nacional de Energía Atómica, Universidad de Buenos Aires, Buenos Aires, Argentina, [16]Geography Institute, Pontificia Universidad Católica de Chile, Santiago, Chile, [17]Saw Science, Invercargill, New Zealand, [18]Laboratoire Interuniversitaire des Systèmes Atmosphériques, Université Paris Cité and University Paris Est Creteil, CNRS, Paris, France, [19]Izaña Atmospheric Research Centre AEMET, Joint Research Unit to CSIC Élimate and Composition of the AtmosphereÏ La Marina 20, Santa Cruz de Tenerife, Spain, [20]Group of Atmosphere, Aerosols and Climate, IPNA CSIC, Tenerife, Spain, [21]Department of R&D, CIMEL Electronique, Paris, France, [22]Cooperative Institute for Research in the Atmosphere, Colorado State University, Fort Collins, CO, USA, [23]Finnish Meteorological Institute, Helsinki, Finland, [24]Earth & Planetary Sciences Department, Institute of Marine Sciences, University of California, Santa Cruz, CA, USA, [25]Institute for a Sustainable Environment, Clarkson University, Potsdam, NY, USA, [26]School of Geography, Earth and Environmental Sciences, University of Birmingham, Birmingham, UK, [27]Energy, Environmental and Chemical Engineering, Washington University, St. Louis, MO, USA, [28]Department of Chemistry, Ghent University, Gent, Belgium, [29]Universidad de Navarra, Instituto de Biodiversidad y Medioambiente BIOMA, Pamplona, Spain, [30]National Institute of Environmental Health Sciences, National Health Research Institutes, Miaoli, Taiwan, [31]Department of Mechanical Engineering, Colorado State University, Fort Collins, CO, USA

Abstract Iron emissions from human activities, such as oil combustion and smelting, affect the Earth's climate and marine ecosystems. These emissions are difficult to quantify accurately due to a lack of observations, particularly in remote ocean regions. In this study, we used long-term, near-source observations in areas with a dominance of anthropogenic iron emissions in various parts of the world to better estimate the total amount of anthropogenic iron emissions. We also used a statistical source apportionment method to identify the anthropogenic components and their sub-sources from bulk aerosol observations in the United States. We find that the estimates of anthropogenic iron emissions are within a factor of 3 in most regions compared to previous inventory estimates. Under- or overestimation varied by region and depended on the number of sites, interannual variability, and the statistical filter choice. Smelting-related iron emissions are overestimated by a factor of 1.5 in East Asia compared to previous estimates. More long-term iron observations and the consideration of the influence of dust and wildfires could help reduce the uncertainty in anthropogenic iron emissions estimates.

Plain Language Summary Human activities, such as smelting and oil combustion, release smoke and particles into the atmosphere. These particles often contain iron, which not only absorbs sunlight,

Key Points:

- Anthropogenic total iron emissions are constrained to a factor of 3 in most global regions using long-term aerosol observations
- The number of sites, interannual variability, and site selection filter can affect the model-observation comparison uncertainty by 15%–50%
- Smelting-related emissions are constrained to a factor of 1.5 using iron oxide observations from East Asia

Supporting Information:

Supporting Information may be found in the online version of this article.

Correspondence to:

T. C. Bond,
tami.bond@colostate.edu

Citation:

Rathod, S. D., Hamilton, D. S., Nino, L., Kreidenweis, S. M., Bian, Q., Mahowald, N. M., et al. (2024). Constraining present-day anthropogenic total iron emissions using model and observations. *Journal of Geophysical Research: Atmospheres*, *129*, e2023JD040332. https://doi.org/10.1029/2023JD040332

Received 3 NOV 2023
Accepted 31 JUL 2024

Author Contributions:

Conceptualization: Sagar D. Rathod, Jeffrey R. Pierce, Tami C. Bond
Data curation: Sagar D. Rathod
Formal analysis: Sagar D. Rathod, Lance Nino
Funding acquisition: Tami C. Bond
Investigation: Sagar D. Rathod, Jeffrey R. Pierce, Tami C. Bond
Methodology: Sagar D. Rathod, Douglas S. Hamilton, Lance Nino, Sonia M. Kreidenweis, Qijing Bian, Natalie M. Mahowald, Andres Alastuey, Xavier Querol, Adina Paytan, Paulo Artaxo, Barak Herut, Cassandra Gaston, Joseph Prospero, Shankararaman Chellam,

Christoph Hueglin, Daniela Varrica, Gaetano Dongarra, David D. Cohen, Patricia Smichowski, Dario Gomez, Fabrice Lambert, Francisco Barraza, Gilles Bergametti, Sergio Rodríguez, Yenny Gonzalez-Ramos, Jenny Hand, Katriina Kyllönen, Patrick Chuang, Philip K. Hopke, Roy M. Harrison, Brenna Walsh, Crystal Weagle, Willy Maenhaut, Yasser Morera-Gómez, Yu-Cheng Chen, Jeffrey R. Pierce, Tami C. Bond
Software: Douglas S. Hamilton, Lance Nino, Sonia M. Kreidenweis, Qijing Bian, Natalie M. Mahowald
Supervision: Jeffrey R. Pierce, Tami C. Bond
Validation: Sagar D. Rathod
Visualization: Sagar D. Rathod, Lance Nino, Jeffrey R. Pierce, Tami C. Bond
Writing – original draft: Sagar D. Rathod, Jeffrey R. Pierce, Tami C. Bond
Writing – review & editing: Sagar D. Rathod, Douglas S. Hamilton, Lance Nino, Sonia M. Kreidenweis, Qijing Bian, Natalie M. Mahowald, Andres Alastuey, Xavier Querol, Adina Paytan, Paulo Artaxo, Barak Herut, Cassandra Gaston, Joseph Prospero, Shankararaman Chellam, Christoph Hueglin, Daniela Varrica, Gaetano Dongarra, David D. Cohen, Patricia Smichowski, Dario Gomez, Fabrice Lambert, Francisco Barraza, Gilles Bergametti, Sergio Rodríguez, Yenny Gonzalez-Ramos, Jenny Hand, Katriina Kyllönen, Hannele Hakola, Patrick Chuang, Philip K. Hopke, Roy M. Harrison, Randall V. Martin, Brenna Walsh, Crystal Weagle, Willy Maenhaut, Yasser Morera-Gómez, Yu-Cheng Chen, Jeffrey R. Pierce, Tami C. Bond

contributing to atmospheric warming, but also serves as a nutrient for phytoplankton in various ocean regions. However, the precise extent of human-induced iron emissions remains uncertain due to a lack of comprehensive monitoring data. In this study, we leverage a global data set of iron observations to refine our estimates of iron emissions attributed to human activities. Additionally, we examine other co-released substances, such as carbon and nickel, to identify specific emission sources of iron. We employ statistical techniques to distinguish human-caused iron emissions from those originating from natural sources like dust and wildfires. Moreover, we utilize iron oxide observations to constrain emissions originating from East Asia and Norway, which are estimated to originate largely from smelting emissions. Through the analysis of long-term data sets, we provide lower and upper bounds to human-caused iron emissions. Furthermore, we investigate the impact of reduced observation numbers and a sparse network on the range of estimated iron emissions. Our findings highlight the critical role of observation quality in accurately assessing iron emissions from human activities.

1. Introduction

Iron-containing aerosol particles affect the atmospheric chemistry of acids (Harris et al., 2012; Kotronarou & Sigg, 1993), absorb and scatter solar radiation (Lafon et al., 2006), enhance biological growth in nutrient-limited waters after deposition (Martin et al., 1990), and are toxic to human health (Wang et al., 2020). Iron is emitted by various sources including dust, wildfires, and anthropogenic combustion (Mahowald et al., 2018). Of these, the anthropogenic component is suggested to exert about +0.5 Wm^{-2} direct radiative forcing over regions with high coal combustion and smelting (Rathod, Bond, et al., 2022; Rathod, Hamilton, et al., 2022). Anthropogenic soluble iron deposition (defined as the sum of soluble iron at emission plus the additional solubilized fraction that is gained during transport due to acidic and organic processing) can sustain over 10% of phytoplankton primary productivity within iron-limited North Pacific Ocean areas (Rathod, Bond, et al., 2022; Rathod, Hamilton, et al., 2022). In other regions, the radiative effects, and effects on oceanic biogeochemistry from anthropogenic sources are thought to be smaller than other iron aerosol sources, although there is a lot of uncertainty in remote ocean regions due to a sparsity of observations (Hamilton et al., 2020). This study aims at constraining present-day anthropogenic total iron emissions using a wide suite of worldwide measurements and an atmospheric iron-transport model (Hamilton et al., 2019).

Chemical transport models are used to simulate the movement and deposition of aerosols and gases, which are then used to estimate the global radiative forcing and ocean biogeochemical feedback. These models rely on emission inventories of gases and aerosols as inputs, simulate their transport (including chemical and physical transformations and deposition), and are evaluated using present-day observations. To assess whether the models are producing accurate results, the modeled concentrations of a species of interest are compared to the observed concentrations (e.g., Mahowald et al., 2009). Model-observation disagreement can be from a wide range of factors, including the emission inventories used, aerosol transport and microphysics, and wet and dry deposition processes (Menut et al., 2007; Smith et al., 2017). Current practice is to match observed concentrations by adjusting the emissions (Hamilton et al., 2020; Matsui et al., 2018), but "correct" modeled concentrations can also be achieved through inadvertent compensating errors in different model processes, such as overly high emissions being offset by overly rapid deposition processes.

Currently, models that simulate the life cycle of iron in the atmosphere tend to underestimate total and soluble iron concentrations over the Southern and Atlantic Oceans, potentially by over two orders of magnitude (Ito et al., 2018, 2019; Myriokefalitakis et al., 2018; Rathod et al., 2020). Recently, Liu et al. (2022) and Ito and Miyakawa (2023) obtained a closer model match with observations by identifying a missing anthropogenic source, which most likely originates in Southern Africa. While the model underestimation in the Southern Ocean has been attributed to underestimated wildfire and anthropogenic emissions, these factors alone do not fully explain the discrepancy. Observations of iron oxide minerals that are largely derived from anthropogenic sources suggest that current estimates of anthropogenic iron contributions in the Southern Ocean may be underestimated by a factor of 5, in contrast to the North Pacific Ocean where estimates are more consistent with observations using isotope markers (Kurisu et al., 2021; Liu et al., 2022; Pinedo-González et al., 2020).

Iron, like many trace element species, has both anthropogenic and natural sources; sources which are expected to evolve differently in the future (Hamilton et al., 2020; Rathod, Bond, et al., 2022; Rathod, Hamilton, et al., 2022).

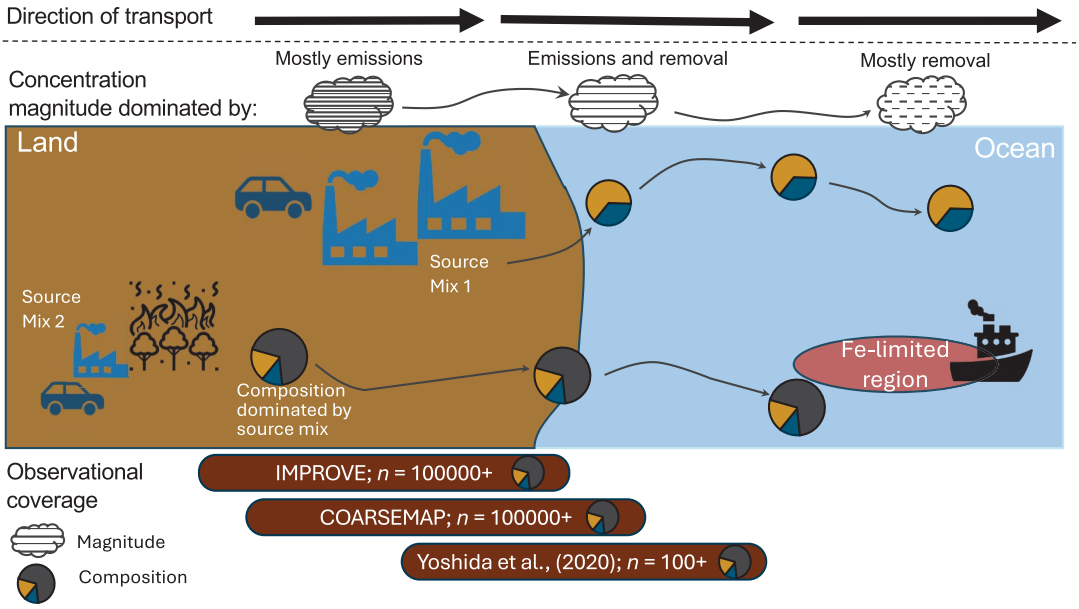

Figure 1. A schematic of the sources, observations, and spatial range covered in this work to evaluate anthropogenic iron emissions. Prior work focused on constraining emissions by only looking at iron concentrations in remote regions, where observations are generally scarce and model errors may be more influenced by deposition and transport than by emissions. This work focuses on the source regions with a multi-species approach using long-term observations. *n* is the number of daily-averaged observations in each site in that observation group. IMPROVE is the US-EPA network of fine aerosol measurements in remote/rural areas in the USA. COARSEMAP is the compilation of global aerosol observations.

This work addresses the questions: What is the current bounded estimate of anthropogenic iron emissions? Which specific emission sources or sectors can be constrained with observations to provide information about how those influences might evolve in the future? How does the shorter duration or lower spatial coverage of observations in some regions affect these estimates?

2. Methods

2.1. Overview

In studies of atmospheric chemistry, "constraining" refers to the process of adjusting a flux, either emission or deposition, or a process to better match observations. It is also a useful exercise for establishing bounds to an emission inventory. For constraining an emission inventory, this is typically done by supplying the inventory to an atmospheric transport model and comparing simulated concentrations to available observations (Cakmur et al., 2006; Martin et al., 2003; Zhu et al., 2013). A correction factor can then be calculated, often as a mean or median of the model-observation comparison and applied to the inventory to improve the match between the model and observations. Some studies use the same inventory in multiple models to determine a universal, rather than model specific, correction factor (Adebiyi et al., 2020; Samset et al., 2014), especially when atmospheric processes dominate the simulated concentration. In this work, we determine an emission correction factor for each region (defined as a continent-level area in this work), including uncertainties. This regional correction factor is defined as the inverse of the median of the model-observation ratio for a single emission inventory. Available observations are limited in time and space and disparate in nature, so we adapt comparison and adjustment methods for each data set, as detailed below. Although the combination of dissimilar methods may appear fragmented, this impression is a consequence of bringing all possible observations to bear on the problem of constraining emissions.

Several factors can impact the accuracy of constraining emissions using model-measurement comparisons, as shown in Figure 1. The locations of observations can affect how much the simulated concentrations are influenced by emission versus transport processes. Observations may be sparse in space and time and may not represent the temporal and spatial aspects of regional concentrations. Although species such as black carbon (Lee et al., 2013)

Table 1
Description of the Analyses Used to Constrain Anthropogenic Iron Emissions in This Paper

Quantity constrained	Observations	Number of locations	Time period	Regions	Distance from source	Analysis
Anthropogenic total iron emissions	COARSEMAP[a]	685 ($PM_{2.5}$) and 185 (PM_{10})	1988–2019	Most in N. America, Europe, Asia, Africa, S. America, Australia	Near	Point-to-point comparisons
Anthropogenic total iron emissions and its sub-sources	US-IMPROVE	171 ($PM_{2.5}$)	1988-2019 (for COARSEMAP; varying by site) 2011–2019 (for PMF)	USA	Near	Positive Matrix Factorization; Point-to-point comparison
Smelting-related iron oxide emissions	Ohata et al. (2018); Yoshida et al. (2020)	5	2017	Japan	Downwind 1000 km	Point-to-point comparison

[a]includes US-IMPROVE.

or dust (Mahowald et al., 2002) are often evaluated using long-term land-based data, modeled iron concentrations have more commonly been compared to observations from ship-based measurements taken over just a few days (Baker & Croot, 2010; Myriokefalitakis et al., 2018), except Ito and Miyakawa (2023) who used 3 months of observations to evaluate modeled iron oxides in Japan. These short sampling periods may not adequately capture the temporal variability of aerosol concentrations, which can vary by many orders of magnitude (Smith et al., 2017). Another challenge in constraining the influence of anthropogenic iron on the Earth system is isolating the anthropogenic component from observed concentrations. Exploring the relationship between co-emitted species can aid in isolating individual source contributions (e.g., Miyakawa et al., 2023).

Figure 1 also shows how near-source observations are emphasized in this study. We evaluate constraints on total anthropogenic iron emissions and their sub-sources. We first describe the emission inventories, atmospheric transport model, and observations used in the study. We identify regions where the simulated anthropogenic contribution to soluble iron affects iron-limited ocean basins because the inputs of anthropogenic sources may be particularly important in these regions. We then compare the anthropogenic subset of iron emissions against observations using two methods: a model filter to identify locations where anthropogenic contributions are predicted to dominate, and Positive Matrix Factorization to quantify the anthropogenic contribution in the observations. We also compare simulated iron oxide concentrations to iron oxide observations from Japan to evaluate smelting emissions in East Asia. Finally, we examine how uncertainties in the representativeness of the observations affect the correction factor and its uncertainty. The observations and analysis methods are summarized in Table 1.

2.2. Emission Inventory

2.2.1. Total Anthropogenic Iron Emissions

Total anthropogenic iron emissions are used directly from Rathod et al. (2020). The global emissions of fine (PM_1) and coarse ($PM_{1\text{-}10}$) mass of anthropogenic iron in Rathod et al. (2020) were 1.1 (0.08–4.6, 95% Confidence Interval) and 1.1 (0.15–6.5, 95% Confidence Interval) Tg/yr, respectively. The fine iron emissions were about an order of magnitude higher than in most previous studies, while the coarse emissions were within the range of most previous studies (Ito, 2015; Matsui et al., 2018; Wang et al., 2015). These emissions were tested in an atmospheric transport model and yielded improvements in model skill for simulating ambient total iron concentrations compared to previous studies (Rathod et al., 2020).

2.2.2. Sector-Specific Emissions

We use the emission output from Rathod et al. (2020) who segregated emissions into major sectors based on source characteristics and solubility. The emission groups are: "Coal": combustion of coal and other solid fuels and were 200 (30–800 95% Confidence Interval) Gg Fe/yr in 2010 in the PM_1 fraction. "Smelt": Emissions from iron and steel, copper, aluminum, zinc, and lead production, including both smelting and sintering, and were 820

(45–3,500) Gg Fe/yr in 2010 in the PM_1 fraction. 'Oil': combustion of heavy fuel oil (HFO), gasoline, diesel, and natural gas emissions; dominated by HFO in boilers and ships. Iron emissions from these sources were 20 (6–55) Gg Fe/yr in 2010 in the PM_1 fraction "Wood": combustion of wood and solid waste and were 55 (2–330) Gg Fe/yr in 2010 in the PM_1 fraction.

2.2.3. Iron Oxide Emissions

Rathod et al. (2020) segregated anthropogenic combustion-iron minerals from coal, wood, oil, and smelting emissions into iron oxides (hematite and magnetite), clays (illite and kaolinite), and iron-sulfates. To estimate hematite (Fe_2O_3) and magnetite (Fe_3O_4) emissions for comparison with the observed iron oxide (FeO_x, sum of hematite and magnetite) mass reported by Yoshida et al. (2018, 2020), we normalized the Fe-as-Fe_2O_3 and Fe-as-Fe_3O_4 masses in the inventory using the chemical mass fractions of $Fe/Fe_2O_3 = 0.7$ and $Fe/Fe_3O_4 = 0.723$.

2.2.4. Natural Sources of Total Iron

Non-anthropogenic sources of iron, dust and wildfires, emit a large amount of total and soluble iron. These two sources affect the locations where anthropogenic contribution to iron dominates and thus affect the model evaluation, as further described in Section 2.5. We model dust and wildfire-related total iron emissions following Hamilton et al. (2019). Dust-iron is estimated by multiplying the emitted mass of dust, which is tracked online in the model, by an iron fraction that depends on the mineralogy of the dust source location (global mean ~3%). Wildfire-iron is estimated by multiplying the wildfire-related black carbon emissions (used from Global Fire Emissions Database version 4s, GFED4s, van der Werf et al. (2017) by observed black carbon-to-iron ratios from various biomes (Hamilton et al., 2019).

2.3. Atmospheric Transport Modeling

2.3.1. Model Setup

Aerosol emissions are transported in the Community Earth System Model's Community Atmosphere Model v6 ("CAM6," Hamilton et al., 2019; Hurrell et al., 2013). The model resolution is 0.94° × 1.25° (latitude *x* longitude) and has 56 hybrid-sigma pressure levels from 1,000 hPa (ground) to 2 hPa. Emissions of anthropogenic species, such as aerosol precursor vapors and primary carbonaceous carbon, are taken from the Coupled Model Intercomparison Project-5 (CMIP5) emission data set (Lamarque et al., 2010), and dust and sea-spray emissions are calculated online. The model is nudged using Modern-Era Retrospective analysis for Research and Applications (MERRA2, Rienecker et al., 2011) offline meteorology so that the different representations of anthropogenic iron-containing aerosol can be compared without a feedback on the meteorology. Unless otherwise specified, each model simulation was run for 18 months starting in 2009 with the first 6 months discarded as the spin-up.

2.3.2. Aerosol Size Treatment

CAM6 uses the Modal Aerosol Module-4 (MAM4, Liu et al., 2016) to track the evolution of aerosol size and composition during its life cycle. Anthropogenic iron emissions are segregated by mass into PM_1 (fine) and $PM_{1\text{-}10}$ (coarse). At the time of emission, 10% and 90% of the anthropogenic PM_1 iron mass are allocated to the Aitken mode and the accumulation modes, respectively, while all $PM_{1\text{-}10}$ is allocated to the coarse mode. As the aerosol particle population grows or shrinks during transport, for example, due to coagulation and condensation/evaporation of vapors, they are reallocated to suitable aerosol size modes.

2.3.3. Solubility Treatment

We run the CAM6 model with the Rathod et al. (2020) total and soluble anthropogenic iron emissions with an updated atmospheric solubility treatment (CAM6-MIMI) module (Rathod et al., 2020). MIMI simulates the atmospheric reactions of iron with atmospheric acids and ligands to estimate the conversion of insoluble to soluble iron during transport (Hamilton et al., 2019). Most soluble iron deposition occurs via wet deposition (Rathod et al., 2020). For the sector-specific solubility simulation described below, we used the Rathod et al. (2020) central fuel solubility.

2.3.4. Simulations

We performed three simulations to estimate the concentrations of anthropogenic total and soluble iron, determine the contribution of anthropogenic sub-sources to these concentrations, and evaluate the contribution of coal combustion and smelting emissions to anthropogenic iron oxide concentrations. The first simulation utilized the CAM6 model with Rathod et al. (2020) anthropogenic iron emissions and the CAM6-MIMI module for all other iron emissions to identify areas where the anthropogenic supply of soluble iron is important in iron-limited ocean waters, defined as those with surface NO_3^- concentrations greater than 4 μM for the central bound and 2 μM for the upper bound (Okin et al., 2011). The soluble iron deposition and iron-limited maps were then overlaid. The total iron concentrations from this simulation, including contributions from dust, wildfires, and anthropogenic sources, were used to compare with observations in Section 2.5.1. In the second simulation, anthropogenic source-specific emissions were transported using CAM6 to identify the sources that contribute most to surface-level concentrations of total and soluble iron, as well as the regions where they have the greatest impact. In the third simulation, the CAM6 model was run with anthropogenic iron oxide emissions to evaluate the contribution of coal combustion and smelting emission sources to total anthropogenic iron, as described in Section 2.5.2.

2.4. Observations

This section summarizes the observations available to constrain anthropogenic iron emissions in various details. Their spatio-temporal coverage and applications are summarized in Table 1.

2.4.1. US-IMPROVE

The US-IMPROVE (Interagency Monitoring of Protected Visual Environments, http://vista.cira.colostate.edu/Improve/improve-data/) network collects and analyzes various metals, organic, and inorganic species using a Teflon filter and X-ray fluorescence (XRF). The network collects 24-hr samples every third day, from midnight to midnight local time (Hand et al., 2012). We use 1988–2019 data for comparison against total iron (Section 2.5.1.1), and only 2011–2019 for comparison against anthropogenic sub-sources (Section 2.5.1.2) to avoid changes in analytical protocols that were implemented starting in 2011 (Solomon et al., 2014).

2.4.2. COARSEMAP

COARSEMAP is a global data set of voluntary contributions (http://www.geo.cornell.edu/eas/PeoplePlaces/Faculty/mahowald/COARSEMAP/), consisting mainly of land-based observations of particulate iron at daily to monthly resolution for periods of more than 1 year. The aerosol samples were analyzed using various methods such as inductively coupled plasma mass spectrometry (ICP-MS) and X-ray fluorescence (XRF), which may lead to differences between samples. Many of the observations in COARSEMAP come from country- or state-level agencies such as the US Environmental Protection Agency, while the rest come from individual research groups. COARSEMAP has global coverage, but most observations are in the USA for $PM_{2.5}$-Fe and in Europe for PM_{10}-Fe (Tables S1, S2, and Table S3 in Supporting Information S1). The following groups and studies contributed to this work (Alastuey et al., 2016; Arimoto et al., 2003, 2006; Artaxo et al., 2002; Barraza et al., 2017; Bergametti et al., 1989; Bozlaker et al., 2019; Bozlaker et al., 2013; Y. Chen et al., 2006; Chuang et al., 2005; Cohen et al., 2004; Dongarrà et al., 2007; Fuzzi et al., 2007; Hand et al., 2017; Hueglin et al., 2005; Kyllönen et al., 2020; Laing et al., 2014; Mackey et al., 2013; Maenhaut, De Ridder et al., 2002; Maenhaut et al., 1996, 2005, 2011; Maenhaut, Fernández-Jiménez, et al., 2002; Maenhaut & Cafmeyer, 1998; Malm et al., 2007; McNeill et al., 2020; Mkoma, Maenhaut, et al., 2009; Mkoma, Wang, & Maenhaut, 2009; Morera-Gómez et al., 2018; Putaud et al., 2010; Putaud et al., 2004; Rodríguez et al., 2011; Salma et al., 1997; Savoie et al., 1993; da Silva et al., 2008; Smichowski et al., 2004; Van Dingenen et al., 2004; Virkkula et al., 1999).

2.4.3. Yoshida et al. (2020) Iron Oxide

Atmospheric iron oxide observations were made using a modified single-particle soot photometer (SP2) (Matsui et al., 2018; Moteki et al., 2017; Ohata et al., 2018; Yoshida et al., 2018) to detect light-absorbing refractory aerosols. The values tabulated by Yoshida et al. (2020) represent emissions from high-temperature combustion activities, mainly smelting and coal combustion (Moteki et al., 2017; Ohata et al., 2018; Yoshida et al., 2018), in East Asian continental outflow plumes (site Hedo, and Fukue), fresh urban pollution (Tokyo and Chiba), and pristine Arctic air (Ny-Ålesund).

2.5. Model Evaluation and Uncertainties

2.5.1. Contribution of Anthropogenic Sources

2.5.1.1. Model Site Selection Filter

We evaluate the anthropogenic total iron concentrations using two site selection filters. The first filter, known as the "dominant-source filter," compares the model to observations only at sites where the modeled anthropogenic iron concentrations in the $PM_{2.5}$ or PM_{10} size range, surpass all other iron sources (i.e., wildfires and dust). This filter ensures that the evaluation is primarily influenced by the anthropogenic component. However, to estimate the uncertainty introduced by this filter selection, we also perform a model evaluation using a more stringent filter requiring a 90% modeled anthropogenic contribution. Although this filter would produce a comparison less influenced by external factors, it applies to only a small number of sites. The uncertainty due to the site selection filter is estimated by comparing the median model-to-observation ratio of the sites selected with the 90% cut-off to the ratio of the sites selected with the dominant-source filter. In both evaluations, we compare modeled surface total iron concentrations from anthropogenic sources, dust, and wildfires to observations of $PM_{2.5}$-Fe and PM_{10}-Fe, using specific mass contributions based on particle size for each case.

2.5.1.2. Positive Matrix Factorization

Measurements can provide an elemental composition that might be used to quantify the contribution of anthropogenic sources. Positive Matrix Factorization (PMF) is a receptor-only, statistical model that seeks groups of associated species (factors) based on the association of elements in the observations, attributes concentration to each factor, and, in the best case, associates each factor with a source or sources (Paatero, 1997; Paatero & Tapper, 1994). It uses no previous information about sources or their characteristics (e.g., Kim et al., 2003), but it must assume that each factor, or that group of associated species, is constant across time scales. PMF has been applied to various real-world cases (Ramadan et al., 2000). Several factors can influence the way species are grouped into factors, and therefore the results of the PMF. One factor is the atmospheric processing of species, such as the oxidation of SO_2 to produce SO_4, which has the effect of altering factors depending on the air-mass age (Yuan et al., 2006). The co-location of emission sources may also result in a factor that combines multiple sources (Chueinta et al., 2000; Clements et al., 2017; Yin et al., 2015). Additionally, PMF is generally used for small air basins rather than an entire continent, and source profiles may vary regionally (e.g., Vecchi et al., 2008), making clear identification of profiles difficult over a large region. For example, emissions linked to heavy fuel oil may have the same spatial distribution as sea salt in coastal areas but be collocated with SO_4 emissions and industrial PM emissions in inland areas.

In this work, we explore the possibility that continental-scale PMF with speciated data could be used to constrain classes of iron emissions within large-scale models. For such an endeavor, it would be unsuitable and computationally expensive to identify factors for individual sites. Rather, PMF was run on the combined data from all IMPROVE sites in the United States. Such combination of sites with likely disparate profiles can often lead to unintelligible results. The selection and processing of IMPROVE observations are described in Text S1 and Table S4 in Supporting Information S1. The final data set consisted of approximately 176,000 observations from 148 sites in the United States. To determine the optimal number of factors for the analysis, the second derivative maximum of the ratio of Q/Qexp was used (Ulbrich et al., 2009); also see Text S1.

2.5.2. Smelting-Related Iron Oxide Emissions

Inventories of iron aerosol that include metal smelting identify it as the largest anthropogenic source of iron aerosol to the atmosphere (Ito & Miyakawa, 2023; Rathod et al., 2020), and most of the material is emitted as iron oxides due to high-temperature oxidation (Rathod et al., 2020). We compare modeled and observed aerosol iron oxide concentrations at four observation sites in Japan and one site in Norway where models and observations indicate that anthropogenic iron oxide sources dominate iron concentrations (Ohata et al., 2018; Yoshida et al., 2018); these iron oxide concentrations, in turn, are dominated by smelting and coal combustion activities. Measured concentrations are limited to the PM_1 fraction and are compared with the sum of modeled Aitken and accumulation-mode iron oxide (hematite and magnetite, Section 2.2).

2.5.3. Uncertainties

The model-observation comparison to obtain a single correction factor by region for the inventory includes many uncertainties. In this section, we describe four uncertainties that affect the correction factor: site selection factor (discussed in Section 2.5.1.1), number of sites, interannual variability, and inter-model variability. We then describe the procedure to combine these uncertainties.

2.5.3.1. Number of Sites

The COARSEMAP data set contains fewer than 20 observation sites for both $PM_{2.5}$ and PM_{10} iron in many regions, except North America and Europe. To estimate the uncertainty introduced by having fewer sites in many regions, we perform a sensitivity analysis on the North American COARSEMAP $PM_{2.5}$-Fe observations, which consist of 527 sites that pass the dominant-source filter. We simulate a lower number of sites by randomly selecting a certain number of sites (n) from the entire data set for that region, determining the median model-to-observation ratio for this subset, and comparing it to the ratio for the whole data set. This process is repeated 500 times for each value of n, and the uncertainty in the median model-to-observation ratio is estimated as the 5th and 95th percentiles. The values of n explored are geometrically spaced in 14 intervals, from $n = 1$ to $n = 527$.

2.5.3.2. Interannual Variability

The model was run for the year 2010, and comparison with observations from other years or a long-term average may introduce bias due to interannual variability (IAV). To estimate the IAV bias, we use the yearly-averaged data from the IMPROVE network for the years 2006–2014 (four years before and after 2010) and compare the modeled 2010 concentrations to each yearly average and the 2006–2014 observed mean. The IAV bias is then calculated as the ratio of the median model-observation ratio for each year to the median model-observation ratio for the 2006-2014 mean. The uncertainty due to IAV is presented as the 5th and 95th percentiles of the obtained ratios for all years. This IAV bias is only applied to regions where more than 20% of the sites have a temporal coverage of 1 year or less. This cut-off is arbitrary but follows an intermediate finding that having at least 2 years of data reduces the IAV bias to 50% of the bias due to having 1 year of data.

2.5.3.3. Inter-Model Variability

We used the Community Earth System Model's CAM6 atmospheric transport model to evaluate the emission inventory. However, selecting any other model (such as GEOS-Chem) would lead to a different model-observation bias because of different aerosol representations and model resolutions (Hamilton et al., 2019; Tsigaridis et al., 2014). To estimate the uncertainty due to different model outputs, we refer to literature where different atmospheric transport models were fed the same aerosol emission inventory and meteorological conditions. Chen et al. (2019) found the inter-model standard deviation to be about 20% of the mean for near-source regions for $PM_{2.5}$ in China. Thus, we assume that about 20% of the model difference from observations can be attributed to model selection.

2.5.3.4. Combined Uncertainty

We assume that the uncertainties discussed above are independent of each other, and combine them in quadrature (e.g., Streets et al., 2003). For the model-observation comparison, we use the inverse of the median of the model-observation comparison as the base correction factor and the 5th and 95th percentiles in its distribution as the 90% Confidence Intervals of the correction factor. We use the same method for the PMF model-observation comparison. For the site selection filter parameter, we use the ratio of the median model-to-observation comparisons in the two filters (dominant source and 90% anthropogenic contribution) filters as is, without using uncertainty bounds to the obtained values. For the number of sites parameter, since the distribution is from 500 random samples, we assume the 5% and 95% percentiles to represent the 90% Confidence Interval of the mean. For the interannual variability parameter, since we compare each year's median model-observation ratio to the 10-year' median model-observation, we perform a bootstrapping analysis and use the 5th and 95th percentiles as the 90% confidence intervals. For the model selection parameter, we use 0.8 and 1.2 as the 5th and 95th percentiles. We then calculate the low and high bounds of the confidence intervals individually based on the low and high estimates of the uncertainties in the individual parameters.

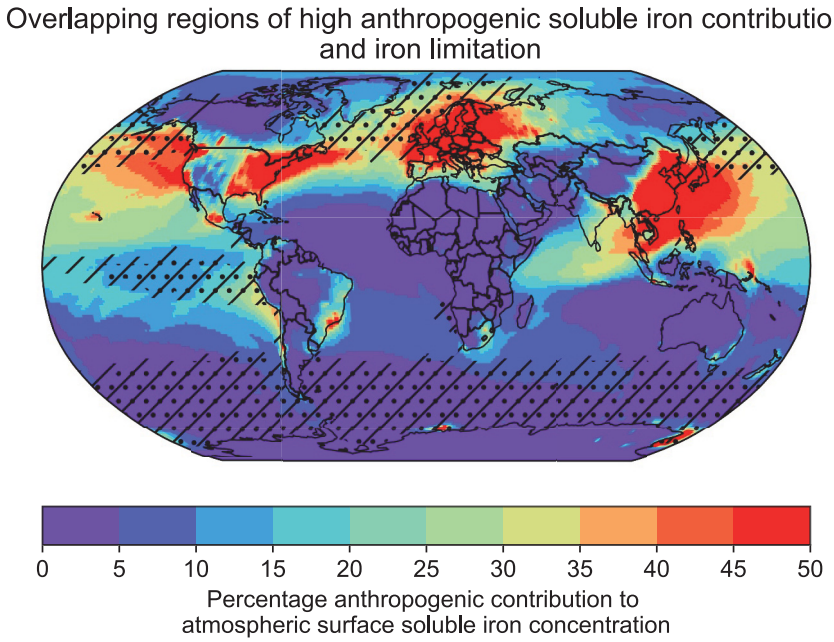

Figure 2. The background shows the percentage anthropogenic contribution to present-day atmospheric soluble iron concentration, and the dots and hatches show central and upper bounds, respectively, of the annual average iron-limitation area.

3. Results

In this section, we first identify the simulated regions where a high anthropogenic contribution to atmospheric soluble iron overlaps with iron-limited oceanic phytoplankton growth areas (Section 3.1.1). This identification is done to identify the regions where the emissions are originating and constrain emissions in those regions, although we present global comparison as well for broader implications of anthropogenic iron as recent studies suggest that they can have a bigger role in the Southern Ocean than previously thought. We then show simulated anthropogenic source-specific contributions to total and soluble iron (Section 3.1.2). In Section 3.2, we evaluate the modeled values against observations for various anthropogenic emission sources in multiple regions. In Section 3.3, we show the influence of various model-observation comparison parameters on the uncertainty in constraining the inventory.

3.1. Regions Where the Anthropogenic Contribution Is Important

3.1.1. Regionality

Figure 2 shows the annual average contribution of anthropogenic soluble iron to total atmospheric soluble iron (dust, wildfires, and anthropogenic) concentration, with dots and hatches representing the central and upper bounds of the area of iron limitation for oceanic phytoplankton growth (see Section 2.3 for the definition of iron limitation). The Rathod et al. (2020) inventory and the CAM6-MIMI model estimate that anthropogenic sources supply 15%–50% of atmospheric soluble iron to the iron-limited North Pacific, Equatorial Pacific, and North Atlantic waters. The westward increasing trend in the percentage of anthropogenic soluble iron across the tropical North Atlantic (from off North Africa, to the Caribbean and Southeastern United States) agrees with observations (Rodríguez et al., 2021). The anthropogenic contribution to atmospheric soluble iron in Fe-limited areas such as the Southern Ocean is less than 15%. We thus focus on North America and East Asia from where anthropogenic emissions originate and influence the iron-limited ocean basins of the North Atlantic and North Pacific oceans, respectively.

3.1.2. Dominant Anthropogenic Sources

Figure 3 shows the simulated contributions of specific anthropogenic sources to surface concentrations of total and soluble iron in the PM_{10} fraction. Smelting and coal combustion are less soluble due to the higher iron oxide

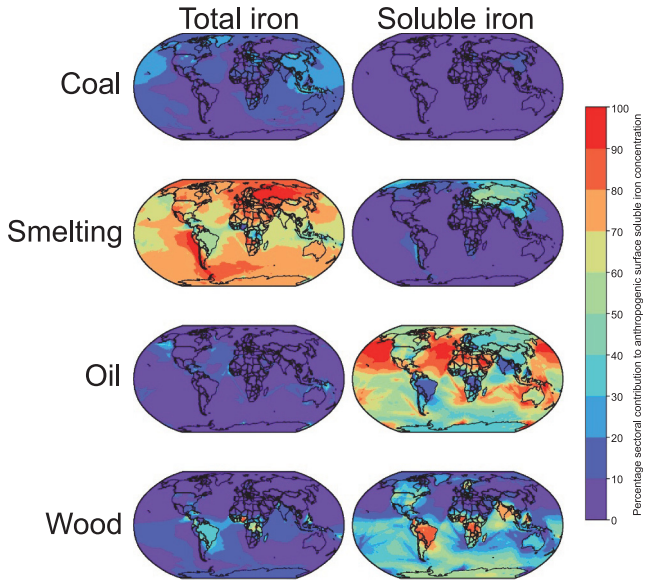

Figure 3. Simulated percentage contributions to $PM_{2.5}$-Fe total (left panel) and soluble (right panel) anthropogenic iron surface concentration by its sub-sources. Note that these maps do not include contributions from dust and wildfire sources of iron.

content in them compared to the higher iron sulfate content in oil and wood combustion aerosols (Rathod et al., 2020). Smelting-related emissions are the dominant source of anthropogenic total iron globally, with contributions to atmospheric surface total iron concentration exceeding 60% in many regions (Ito & Miyakawa, 2023; Rathod et al., 2020). Coal combustion is another significant source of anthropogenic total iron in industrial areas of North America, East Asia, and Europe. Heavy fuel oil and other liquid-fuel combustion in industrial and shipping sectors and wood combustion in industrial and residential sectors are the main contributors to soluble iron, particularly over iron-limited ocean waters. Other studies suggest either oil and wood (Wang et al., 2015) or smelting (Ito & Miyakawa, 2023; Liu et al., 2022) as dominant soluble iron sources. Further information on the solubility of emissions from these sources would aid in reducing this uncertainty.

3.2. Comparison With Observations

3.2.1. Anthropogenic Total Iron Emissions

3.2.1.1. Global: Model-Observation Comparison at Sites With High Anthropogenic Influence

We first discuss the model-observation comparison using the "dominant source" filter in which sites are used for comparison only where the modeled anthropogenic contribution is the highest among the sum of all sources (i.e., anthropogenic combustion, wildfires, and dust). Figures 4a and 4b show boxplots of the model-observation comparison for $PM_{2.5}$ and PM_{10} fractions, respectively. Over 90% of the modeled values are within an order of magnitude of the observations for both PM sizes, with over 50% of sites within a factor of 5. Maps of modeled concentrations and observation locations are shown in Figures S1 and S2 in Supporting Information S1 for $PM_{2.5}$ and PM_{10}, respectively. Table S3 in Supporting Information S1 defines the continent boundaries used for model-observation comparison. Most of the $PM_{2.5}$-Fe observations are in North America, while most of the PM_{10}-Fe observations are in Europe. Observations of coarse mass, which represents 50% of emissions and 30% of concentration over remote oceans in the model (Rathod et al., 2020), are relatively poorly represented, with only 20% of the number of $PM_{2.5}$-measuring sites. In Europe, the modeled concentrations of $PM_{2.5}$-Fe were overestimated by a factor of 1.2, while the PM_{10}-Fe was underestimated by a factor of 2.

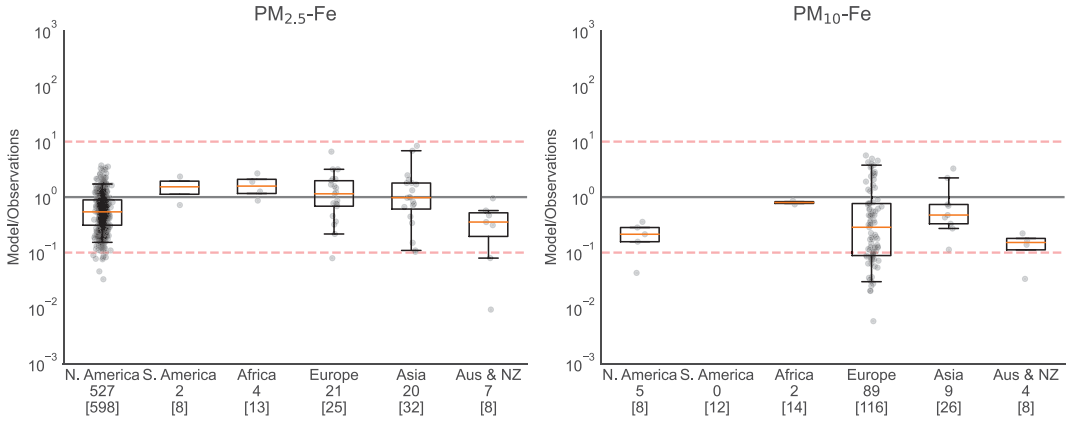

Figure 4. Model-observation comparison of $PM_{2.5}$-Fe (a) and PM_{10}-Fe (b) annual average iron concentration in various regions. Comparison is performed and shown only for sites where the anthropogenic contribution in each size range is the highest of the three classes of atmospheric sources (dust, wildfires, and anthropogenic combustion). Each dot represents the ratio of the modeled 2010 mean concentration to the observed temporal mean concentration for each site. Values below the region name show the number of observation sites used in the evaluation. Values in brackets show the total number of sites in each region. Whisker length shows the 5th to 95th percentiles.

Two continental emission regions contribute to most of the soluble iron deposition in the North Atlantic and North Pacific Oceans: North America and East Asia, respectively (Hamilton et al., 2019). Shipping emissions within these oceanic regions also contribute to deposition (e.g., Ito, 2015). Emissions from western South America contribute about 15% of total atmospheric soluble iron to the iron-limited Equatorial Pacific Ocean, with higher soluble iron fractions close to the continent. Of the three source regions discussed here, South America and Asia have many fewer sites (2 and 29, respectively) that passed the dominant source filter compared to North America with 527 sites. The model underestimates concentrations over North America by a factor of 2 and overestimates concentrations by a factor of 1.1 over Asia for $PM_{2.5}$-Fe and a factor of 5 and 2 respectively for PM_{10}-Fe. We infer the following correction factors and their uncertainties as the median and 5th and 95th percentiles of the inverse of the model-observation ratio: 1.9 (0.6–6.6) for North America, 0.7 (0.4–1.25) for South America, 0.6 (0.4–1.1) for Africa, 0.9 (0.3–4.6) for Europe, 1 (0.1–9.1) for Asia, and 2.8 (1.2–33.0) for Australia/New Zealand.

3.2.1.2. Positive Matrix Factorization Results for IMPROVE Sites

PMF Factors: PMF produces factor profiles, or groups based on the association of elements in the observations. The analysis of the optimal number of factors (Section 2.5.1.2) suggested that either 9 or 10 factors were optimal. We tentatively assigned each factor to a source group based on existing knowledge about its contribution to key, representative species (Figures S3 and S4 in Supporting Information S1). For example, a factor with a dominant contribution of crustal elements such as Al, Si, and Ti was identified as "Dust." The PMF analysis identified a dust source profile that was relatively constant regardless of site selection, and consistent with observed dust source profiles (Table S7 in Supporting Information S1). However, the PMF analysis was not as successful in identifying consistent profiles for other sources across the entire United States as would be expected given the diversity of profiles from the likely source types. For example, we identified and labeled a potential "biomass burning" factor based on richness in K; and an "oil combustion" factor due to contributions from V, Ni, and SO_4. However, the composition of these factors was not consistent across the entire USA, and the ratio between elements in each factor and iron was dissimilar to that in measured source profiles (Tables S5 and S6 in Supporting Information S1). This discrepancy may be due to the inability of PMF to generalize source profiles across the country. Although SO_4 is often used to identify the influence of coal combustion in PMF, the spatial distribution of the factor contributing most to SO_4 was dissimilar to that of iron emissions from coal combustion, possibly because SO_4 occurs through secondary formation in the atmosphere and iron occurs in primary aerosol.

In summary, the nationwide PMF analysis of iron emissions in the United States resulted in one distinct factor from dust, while other sources could not be clearly separated (Table S8). Although PMF can aid in identifying sources in specific air basins, it was less useful for constraining source contributions on the continental scales required for biogeochemical impacts. Non-dust iron separated by PMF includes both anthropogenic combustion sources and natural wildfires, and we used this group for comparison with the modeled concentrations. We find that the modeled concentrations of both anthropogenic and anthropogenic + wildfire emissions were higher than the non-dust-Fe concentrations in PMF for about 85% of the sites in the United States, and about 97% of the sites were within an order of magnitude (Figure 5). The simulated wildfire contribution was approximately 30% of the anthropogenic component in the United States (Hamilton et al., 2019; S. D. Rathod et al., 2020). The median model-to-observation ratio was 1.7 for the anthropogenic case and 2.3 for the anthropogenic + wildfire case.

3.2.1.3. Total Iron and PMF Comparison

The modeled concentrations underestimate the overall amount of $PM_{2.5}$-Fe, or the sum of anthropogenic combustion, wildfires, and dust when compared to total iron from the COARSEMAP data set (Figure 4a). However, the model overestimates the anthropogenic combustion and wildfire components compared to the PMF analysis in the IMPROVE data set (Figure 5). There are several potential reasons for this contrast in North America. First, dust dominates total iron, and prior research (e.g., Kok et al., 2021) has shown that models may underestimate fine and coarse dust over North America and thus potentially dust-iron, so that total iron would be underestimated and anthropogenic iron would be overestimated (Figure S5 in Supporting Information S1). Second, the filter used in the analysis does not completely eliminate the influence of iron from dust and wildfires, which could lead to a bias in the estimates of the anthropogenic component. Using a site-selection filter that more confidently isolates sites with high anthropogenic contributions ("Anthro >90%") reduces the model underestimation of total-iron observations and narrows the gap between the median model-observation ratio in COARSEMAP and PMF (Section 2.5.1.1 and Section 3.3.1). Finally, there is a possibility that PMF may misattribute a non-trivial amount of

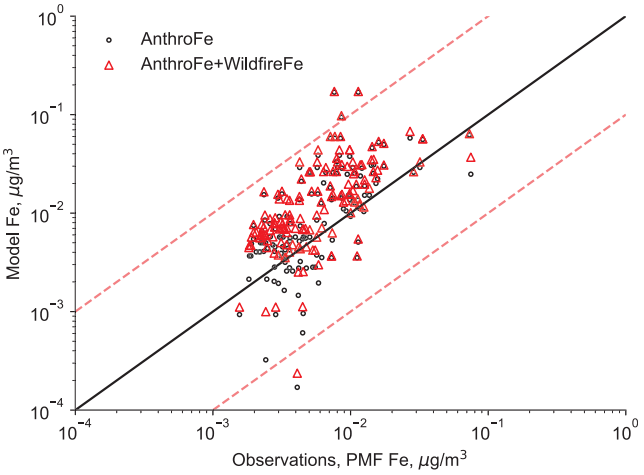

Figure 5. Model anthropogenic (black) or model anthropogenic + wildfire (red) and observed (non-dust Fe in PMF) iron concentrations in the $PM_{2.5}$ size fraction. Each dot represents a USA-IMPROVE site used for PMF analysis. The non-dust-Fe component is identified as the total minus the dust-Fe component and is used here instead of individual PMF factors because of the higher confidence in PMF dust-Fe than other factors.

anthropogenic and wildfire iron to dust, leading to a higher dust contribution and lower anthropogenic contribution in the observations than in the model. Overall, while the model is likely underestimating dust compared to observations, it may have a smaller uncertainty in representing the anthropogenic contribution.

3.2.2. Anthropogenic Iron Oxide Emissions

Smelting contributes about 80% of global anthropogenic emissions of iron oxide, which are estimated as 1.4 Tg/yr (0.1–6.0 Tg/yr, 95% confidence interval (CI), Rathod et al., 2020). For consistency with the only observations, which are made by the SP2 instrument (Yoshida et al., 2020), we compare the PM_1 fraction instead of $PM_{2.5}$ as discussed earlier. The fine iron oxide emissions from East Asia (China, Taiwan, Hong Kong, S. Korea, and N. Korea) were about 0.6 Tg/yr (central estimate), which is near the upper estimate of 0.5 Tg/yr in previous estimates (Ohata et al., 2018; Yoshida et al., 2018) made using the observed relationship between iron oxide and Black Carbon in the outflow from that region.

Anthropogenic sources dominate the surface iron oxide concentration in East Asia's industrial regions (Figure 6a. Electron microscope analyses of particle morphology by Yoshida et al. (2020) and Moteki et al. (2017) identified submicron particles as being of anthropogenic origin, primarily occurring as magnetite. Magnetite is a form of iron oxide that is produced only during high-temperature oxidation of iron, a process typically found in smelting and coal power plants. Furthermore, the small size (<0.3 μm) of these particles and their co-emission with species like black carbon and carbon monoxide corroborate their anthropogenic origins. The model overestimates iron oxide concentration (Figure 6b) near sources by a factor of 3 at Fukue, a factor of 1.5 at all other Japanese sites, and underestimates by an order of magnitude in Ny-Ålesund, which is the only location outside of Japan and is in the Arctic North Atlantic. The modeled values in Figure 6b include only anthropogenic iron oxides, but the difference from total iron oxide, including dust, is negligible (Figure S6 in Supporting Information S1). The overestimation factors of 1.5–3 are within the range determined for total iron (Section 3.2.1). However, the distance between the emission region and the observation sites is greater than in the IMPROVE and COARSEMAP data sets (which are country-level) for this comparison, and largest for the Ny-Ålesund site, so uncertainties in deposition and transport are also greater for the comparison of iron oxide.

Our best estimate of anthropogenic iron oxide (hematite and magnetite) emissions from East Asia is 0.4 Tg/yr, determined as the a priori estimate of 0.6 Tg/yr divided by 1.5, the factor of overestimation. If an equal

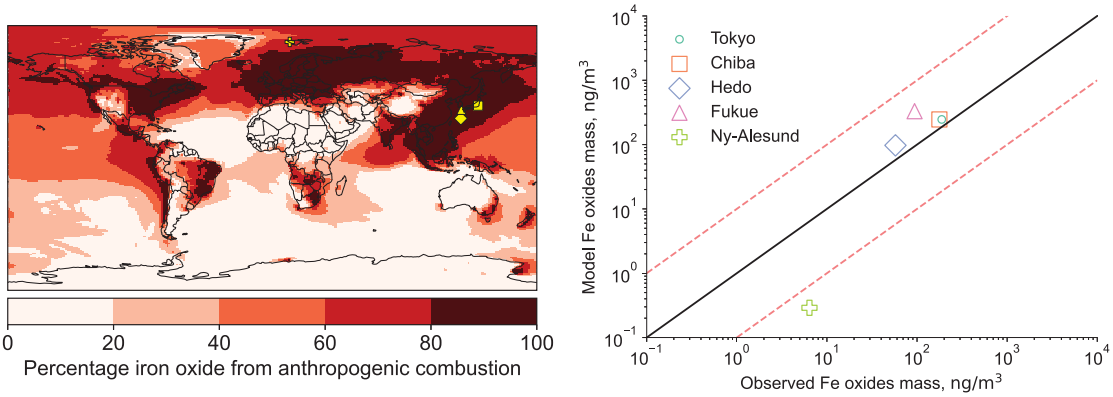

Figure 6. (a) Percentage contribution of fine anthropogenic iron oxides to total fine (anthropogenic + dust) iron oxides. Yellow markers show the observation locations and (b) Model-observation comparison of fine iron oxides at monthly averages in five ground-based sites. Observations are from Yoshida et al. (2020).

Table 2
Summary of Regional Model Evaluation for $PM_{2.5}$-Fe

Region	Filter	n	Base correction factor	Uncertainty (as multipliers to the scale factor)					Combined uncertainty in correction factor (absolute, 90th CI)
				Mod/Obs spread	IAV	# Of sites	Atm. Model[a]	Site selection filter	
North America	Dominant source	527	1.84	**0.3–3.59**	1.00	1.00	0.8–1.2	1.30	1.33–6.65
	>90%Anthro	220	1.22	**0.36–4.15**	1.00	1.00	"	1.00	0.82–5.07
	PMF	148	0.45	**0.31–4.38**	1.00	0.95–1.05	"	1.00	0.32–1.97
South America	Dominant source	2	0.65	0.68–1.92	0.85–1.20	**0.30–2.50**	"	1.30	0.53–1.83
Africa	Dominant source	4	0.63	0.62–1.71	0.85–1.20	**0.50–2.00**	"	1.30	0.41–1.45
Europe	Dominant source	21	0.87	**0.36–5.32**	1.00	0.75–1.40	"	1.30	0.63–4.66
Asia	Dominant source	20	1.02	**0.14–8.99**	1.00	0.75–1.40	"	1.30	0.93–9.19
Aus/NZ	Dominant source	7	2.81	**0.43–11.74**	1.00	0.50–2.00	"	1.30	2.21–33.15

Note. Uncertainties are absolute multipliers and are shown as 5–95th percentiles. The Correction Factor is the factor by which scaling the inventory in that region should lead to a better model-observation comparison. The cumulative uncertainty in the Correction Factor is shown as 90% CI. Parameters representing the highest uncertainty in a region are in bold. IAV = Interannual variability. Atm. Model = Uncertainty due to using only one atmospheric model for the simulations. [a]Applied to all regions, from Chen et al. (2019).

overestimation factor is applied to the subcategory of smelting and coal combustion, the anthropogenic iron emissions from smelting and coal combustion are around 0.3 Tg/yr, accounting for the fact that iron oxides are 72% iron.

3.3. Adjusted Inventory With Uncertainties

In this section, we develop a new best estimate for the inventory, considering all available observations. Table 2 summarizes central adjustments to the inventory and their uncertainties in each region for $PM_{2.5}$-Fe, and these adjustments are detailed in the following sections. We quantify each adjustment using a Correction Factor, or the factor by which scaling the inventory would yield a median model-observation ratio of 1 in that region. Uncertainties of 5% and 95% percentiles are given in the table as multipliers to the Correction Factor. The Base Correction Factor, obtained from Figure 4a, is the median of the model-observation ratios by region. The uncertainty in the Base Correction Factor is then calculated by adding the uncertainties due to model-observation spread, site selection criteria, interannual variability, number of sites, and atmospheric model selection in quadrature. Each of these uncertainties is presented in the table as a value to be multiplied by the Base Correction Factor. The resulting combined uncertainty in the correction factor is shown as an absolute range.

3.3.1. Site Selection Filter

We used a "dominant-source" filter to select sites for comparison in the evaluation of anthropogenic total iron emissions. However, this filter does not exclude sites with considerable iron concentrations from dust and wildfires, which could affect the model-observation ratio for total iron if those sources are overestimated or underestimated in the model. We compared the distribution of model-observation ratios for $PM_{2.5}$-Fe in the North America observational data using a stricter filter where the modeled anthropogenic contribution was more than 90% of atmospheric iron. The results showed that the median model-observation ratio for the "90% cutoff" filter is a factor of 1.3 higher than that obtained using the dominant-source filter, indicating that the underestimation of dust and wildfire emissions most likely influenced the comparison (Figure 7a). However, using the stricter filter excluded 60% of the sites in the United States and 70% of the sites outside the United States. Thus, to reflect the influence of dust and wildfire emissions on the model-observation comparison, the overall model-observation ratio (obtained using the dominant source filter) for North America should be increased by a factor of 1.3. We also apply the same factor of 1.3 to other regions assuming that dust and wildfire influence is similar.

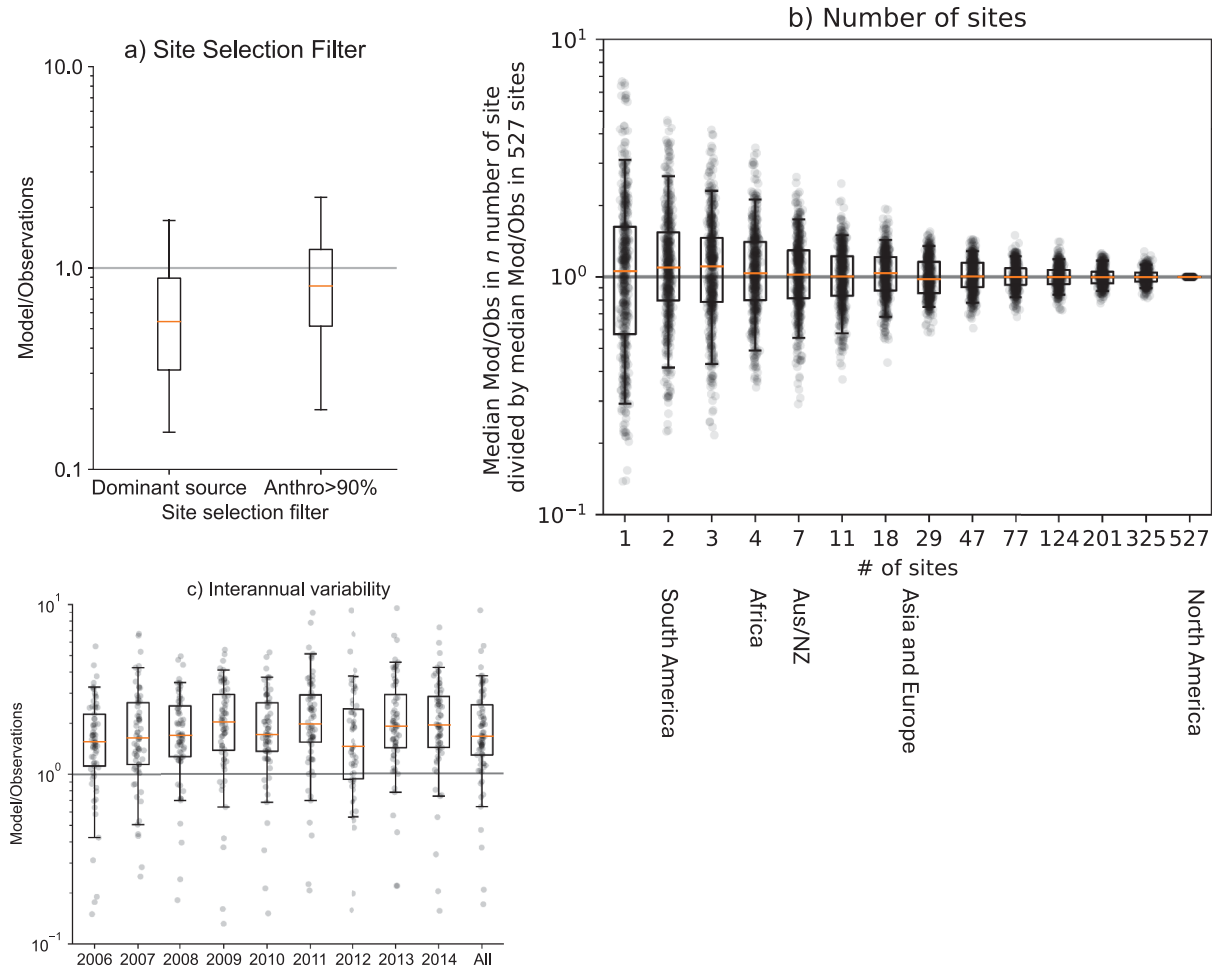

Figure 7. (a) Distribution of the model-observation ratios in the North American COARSEMAP sites for $PM_{2.5}$ total iron concentrations with the two filters described in Section 2.5.1.1. (b) Distributions of total iron concentrations shown as the ratio of the median model-to-observation ratio from a random selection of n sites and the median model-to-observation ratio of all sites Distribution is shown from 500 simulations. (c) Comparison of modeled 2010 values against individual years from 2006 to 2014 and the mean of those years for North America IMPROVE $PM_{2.5}$-Fe observations. The whisker length in all the plots is 5th-95th percentiles.

3.3.2. Number of Sites

Figure 7b analyzes uncertainty caused by a limited number of regional observation sites, using the COARSEMAP data set over North America. Each dot represents the ratio between the median model-to-observation ratio from a random selection of n sites, simulating a smaller network, and the median model-to-observation ratio of all sites. The data and boxplot for each value of n show the results of 500 such simulations. When the number of sites is below 3, the inferred model-to-observation ratios vary by as much as a factor of 3 (5–95th percentiles); however, the uncertainty diminishes rapidly with an increasing number of sites, falling to about 30% for about 20 sites. We apply the following uncertainty factors (as 5th and 95th percentiles) based on the number of sites in each region: 1 for North America ($n = 527$), 0.3–2.5 for South America ($n = 2$), 0.5–2 for Africa ($n = 4$), 0.75–1.4 for Europe ($n = 21$), 0.75–1.4 for Asia ($n = 20$), and 0.5–2 for Australia/New Zealand ($n = 7$). This finding assumes that the spatial variability in different regions is like the variability in North America.

3.3.3. Interannual Variability

Observed concentrations of iron may not accurately reflect long-term averages if the measurement period is short. The effect of duration can be seen in Figure 7c, which shows the ratio of the median model-to-observation ratio

for each year and the median model-to-observation ratio of the mean of 2006–2014 for sites in North America IMPROVE $PM_{2.5}$-Fe observations. This distribution demonstrates the uncertainty of comparing any given year to a long-term average using the model. The median model-to-observation ratio in a year's comparison can range from a factor of 0.85–1.2 compared to the median model-to-observation in of long-term comparison. In North America, South America, Africa, Europe, Asia, and Aus/NZ, there are 3%, 25%, 43%, 18%, 10%, and 13%, respectively, of $PM_{2.5}$-Fe sites with one or fewer years of temporal coverage. We apply an uncertainty range of 0.85–1.2 (as the 5th and 95th percentiles) only to South America and Africa, due to their higher fraction of sites with limited temporal coverage. For other regions, this uncertainty range is not applied.

3.3.4. Combined Uncertainty

The Correction Factor range in Table 2 represents the combined effect of all uncertainties and is given as a 90% confidence interval around the Base Correction Factor. The model-observation spread is the largest uncertainty in North America, Europe, Asia, and Australia/New Zealand while the number of sites is the largest uncertainty in South America and Africa. The site selection uncertainty is the second largest uncertainty in all regions. In all regions except North America and Australia/New Zealand (where the inventory is underestimated even with uncertainty), the Correction Factor range varies from less than one to above one, indicating that the initial estimate is usually within the range of uncertainty.

The variability in model-observation spread has many unknown causes including spatial misrepresentations in the inventory or model (Cakmur et al., 2006; Martin et al., 2003; Zhu et al., 2013). Regions with few sites do not capture this variability and thus the uncertainty attributed to the model-observation spread appears to be low in those regions. The "number of sites" uncertainty offsets this model-observation variability in those regions. However, other regions might have more spatial heterogeneity in emission sources and contributions than the US, which was used to determine these uncertainties. For example, while 10 sites can capture the USA's spatial variability to about 20% uncertainty, 10 sites might not be able to capture the same amount of variability for all of Asia (that includes the Middle East, Russia, India, and China) or Africa. Thus, our treatment of these two uncertainties may still underestimate the total uncertainty.

It would be ideal to perform a similar analysis for coarse iron particles (PM_{10} minus $PM_{2.5}$) to estimate the uncertainty in these emissions. Coarse particles contain about 50% of total anthropogenic iron emissions and 30% of soluble anthropogenic iron emissions (Rathod et al., 2020). However, there are few measurements of iron in coarse particles, making it difficult to estimate the uncertainty in PM_{10}-Fe using observational data. Even if measurements were available, the uncertainty in the comparison is likely to be higher than the uncertainty in $PM_{2.5}$-Fe due to the uncertain contribution of dust and wildfires that dominate the coarse iron mass (Hamilton et al., 2019; Myriokefalitakis et al., 2018). Nevertheless, the contribution of coarse iron to the remote ocean is lower than that of $PM_{2.5}$-Fe due to its limited ability to be transported over long distances (Rathod et al., 2020).

3.4. Implications

The constraining exercise described above suggests bounds for the anthropogenic total iron emissions in several regions. Total iron is important for direct radiative forcing, and soluble iron for oceanic biogeochemistry. Since the radiative and biogeochemistry impacts of anthropogenic iron are dominant over East Asia, and the North Pacific and North Atlantic, respectively (Rathod, Bond, et al., 2022; Rathod, Hamilton, et al., 2022), we discuss the implications of the constraining procedure for emissions from source regions of East Asia and North America. We compare the constrained emission estimates, in which a Correction Factor with uncertainty is applied to the central estimate of emission rate in each region, with a priori emission estimates. We did not apply the Correction Factor to other regions. Even though the model might over- or underestimate in some sub-regions, we discuss the continent-wide uncertainty to focus on the broader implications of this work on biogeochemical and radiative effects.

The estimated uncertainty in the anthropogenic total iron emissions in the $PM_{2.5}$ fraction from Asia, which includes the Middle East, Russia, India, China, East Asia, and Southeast Asia, is 0.72–7.2 Tg/yr (90% CI) with a median estimate of 0.8 Tg/yr. The a priori estimates of anthropogenic total iron emissions from Asia are about 0.8 (0.15–4) Tg/yr, or around 75% of the global total (Rathod et al., 2020). The uncertainty based on observational constraints suggests that the probable lower and upper bounds could be higher than estimated in the a priori inventory. However, iron oxide observations suggest that the central bound could be lower by a factor of 1.5 for

East Asian smelting and coal combustion emissions, which dominate the radiative effects. This is consistent with the model-observation comparison at the two sites in China, where the model overestimates by a factor of 2. This suggests that the direct radiative effect in East Asia could be lower than the estimated 0.5 Wm^{-2} averaged over the region (S. D. Rathod, Bond, et al., 2022; Rathod, Hamilton, et al., 2022). Although the East Asian soluble iron flux is believed to support about 10% of North Pacific Ocean phytoplankton productivity, it was not possible to determine the dominant sources (heavy fuel oil and wood combustion) due to a lack of speciated data.

The estimated anthropogenic iron emissions over North America could be 0.18 (0.1–0.6, 90% CI) Tg/yr, a factor of 1.8 higher compared to the a priori estimates of 0.1 (0.02–0.5, 90% CI) Tg/yr when the dominant source filter is used. For the ">90% Anthropogenic" filter, the base correction factor is 1.22, which reinforces that the model currently underestimates anthropogenic emissions. The a posteriori central estimate could be as low as 0.05 Tg/yr based on the PMF comparison. Since the direct radiative effects of anthropogenic combustion iron in the USA are small (<0.1 Wm^{-2}), the uncertainty of a factor of 2 in its total iron emissions does not significantly impact the overall radiative effects compared to those from other anthropogenic species such as black carbon and sulfur dioxide. However, the North American contribution to soluble iron in the North Atlantic Ocean is non-trivial and supports 5%–10% of phytoplankton productivity (Rathod, Bond, et al., 2022; Rathod, Hamilton, et al., 2022). The sources of soluble iron emissions such as heavy fuel oil and wood combustion were not constrained due to the relatively small (<1%) contribution of these sources to total iron, as well as the limitations of PMF in resolving site-specific source contributions in a large data set like IMPROVE.

4. Summary

Anthropogenic iron forms an integral part of the input to the models that estimate iron's present-day atmospheric and oceanic cycling, yet its emission estimates remain unconstrained (Ito & Miyakawa, 2023; Rathod, Bond, et al., 2022; Rathod, Hamilton, et al., 2022). In this work, we used an atmospheric transport model, an anthropogenic iron emission inventory, and long-term near-source observations from various regions along with Positive Matrix Factorization to evaluate the modeled concentrations. The major findings of this work are:

- The modeling finding suggests that among anthropogenic sources, coal and smelting are the main contributors to total iron, while oil and wood combustion are the main sources of soluble iron. However, accurate source apportionment is required to better understand source contributions in different regions (e.g., Miyakawa et al., 2023).
- The model underestimates total iron concentration (dominated by anthropogenic contribution) compared to observations of $PM_{2.5}$-Fe over Australia/NZ and overestimates in South America, Africa, Europe, and Asia. Over North America, a comparison with IMPROVE and other observations suggests that the anthropogenic emissions could be between a factor of 0.5 and 2 compared to the a priori estimates.
- Anthropogenic $PM_{2.5}$-Fe iron emissions are constrained (median correction factor) to a factor of 2 in all regions except in Australia/NZ where it is within a factor of 3.
- The dominant cause of uncertainty in anthropogenic $PM_{2.5}$-Fe varies by region: model-observation spread is the dominant uncertainty in North America, Europe, Asia, and Australia/New Zealand, whereas the number-of-sites parameter is the dominant uncertainty in South America and Africa.
- PMF was able to reproduce robust dust source profiles when data from 148 sites from the contiguous USA were lumped. However, performing PMF on continent-wide observational data did not provide a robust resolution of anthropogenic sources among the non-dust aerosol. Thus, combining data from sites likely to have significantly different characteristics is generally not recommended.
- Simulated anthropogenic total iron concentrations are overestimated by about a factor of 2 when compared with non-dust-Fe (Total-Fe minus dust-Fe) values from PMF over the USA.
- As few as 10 sites in a continent can aid in constraining simulated concentrations over that region to a factor of 2, assuming the regional variability in iron concentrations is similar to that in the USA.
- East Asian iron oxide emissions, dominated by smelting, are overestimated by a factor of about 1.5 (upper bound of 3), suggesting that radiative forcing attributable to these emissions is also overestimated.
- The total-iron component affects direct radiative forcing, and the soluble component affects biogeochemistry. However, because the soluble iron component is emitted from sources (oil and wood combustion) that do not emit considerable total iron (coal combustion and smelting), they could not be isolated and identified even in speciated observations.

Data Availability Statement

The following data are uploaded to Zenodo.org (Rathod, 2023): (a) Anthropogenic, dust, and wildfire concentration and deposition fields for particulate total and soluble iron (as netCDF), (b) Anthropogenic sectoral concentration and deposition fields for total and soluble iron (as netCDF), (c) PMF-derived total and dust-Fe factors by site (as CSV), and (d) Anthropogenic and dust iron oxide concentration fields (as netCDF).

Acknowledgments
SDR and TCB were supported by the United States Department of Energy (DE-Sc0016362) Collaborative Proposal "Fire, Dust, Air, and Water: Improving Aerosol Biogeochemistry Interactions in ACME." DSH gratefully acknowledges support from NASA (Grant 80NSSC24K0446). We would like to acknowledge high-performance computing support from Cheyenne https://doi.org/10.5065/D6RX99HX; Computational and Information Systems Laboratory, 2017) provided by NCAR's Computational and Information Systems Laboratory, sponsored by the National Science Foundation. RVM acknowledges support from NSF (Grant 2020673). Iron measurements in Houston, Texas were made possible by grants from the Texas Air Research Center to SC. This work contributes to the Scientific Committee on Oceanic Research International Working Group 167: Reducing Uncertainty in Soluble Aerosol Trace Element Deposition. CJG would like to thank NASA MRI Grant 2215875.

References

Adebiyi, A. A., Kok, J. F., Wang, Y., Ito, A., Ridley, D. A., Nabat, P., & Zhao, C. (2020). Dust Constraints from joint Observational-Modelling-experiMental analysis (DustCOMM): Comparison with measurements and model simulations. *Atmospheric Chemistry and Physics*, *20*(2), 829–863. https://doi.org/10.5194/acp-20-829-2020

Alastuey, A., Querol, X., Aas, W., Lucarelli, F., Pérez, N., Moreno, T., et al. (2016). Geochemistry of PM_{10} over Europe during the EMEP intensive measurement periods in summer 2012 and winter 2013. *Atmospheric Chemistry and Physics*, *16*(10), 6107–6129. https://doi.org/10.5194/acp-16-6107-2016

Arimoto, R., Duce, R. A., Ray, B. J., & Tomza, U. (2003). Dry deposition of trace elements to the western North Atlantic. *Global Biogeochemical Cycles*, *17*(1). https://doi.org/10.1029/2001GB001406

Arimoto, R., Kim, Y. J., Kim, Y. P., Quinn, P. K., Bates, T. S., Anderson, T. L., et al. (2006). Characterization of Asian dust during ACE-Asia. *Global and Planetary Change*, *52*(1), 23–56. https://doi.org/10.1016/j.gloplacha.2006.02.013

Artaxo, P., Martins, J. V., Yamasoe, M. A., Procópio, A. S., Pauliquevis, T. M., Andreae, M. O., et al. (2002). Physical and chemical properties of aerosols in the wet and dry seasons in Rondônia, Amazonia. *Journal of Geophysical Research*, *107*(D20), LBA49-1–LBA49-14. https://doi.org/10.1029/2001JD000666

Baker, A. R., & Croot, P. L. (2010). Atmospheric and marine controls on aerosol iron solubility in seawater. *Marine Chemistry*, *120*(1), 4–13. https://doi.org/10.1016/j.marchem.2008.09.003

Barraza, F., Lambert, F., Jorquera, H., Villalobos, A. M., & Gallardo, L. (2017). Temporal evolution of main ambient $PM_{2.5}$ sources in Santiago, Chile, from 1998 to 2012. *Atmospheric Chemistry and Physics*, *17*(16), 10093–10107. https://doi.org/10.5194/acp-17-10093-2017

Bergametti, G., Gomes, L., Coudé-Gaussen, G., Rognon, P., & Le Coustumer, M.-N. (1989). African dust observed over Canary Islands: Source-regions identification and transport pattern for some summer situations. *Journal of Geophysical Research*, *94*(D12), 14855–14864. https://doi.org/10.1029/JD094iD12p14855

Bozlaker, A., Buzcu-Güven, B., Fraser, M. P., & Chellam, S. (2013). Insights into PM10 sources in Houston, Texas: Role of petroleum refineries in enriching lanthanoid metals during episodic emission events. *Atmospheric Environment*, *69*, 109–117. https://doi.org/10.1016/j.atmosenv.2012.11.068

Bozlaker, A., Prospero, J. M., Price, J., & Chellam, S. (2019). Identifying and quantifying the impacts of advected North African dust on the concentration and composition of airborne fine particulate matter in Houston and Galveston, Texas. *Journal of Geophysical Research: Atmospheres*, *124*(22), 12282–12300. https://doi.org/10.1029/2019JD030792

Cakmur, R. V., Miller, R. L., Perlwitz, J., Geogdzhayev, I. V., Ginoux, P., Koch, D., et al. (2006). Constraining the magnitude of the global dust cycle by minimizing the difference between a model and observations. *Journal of Geophysical Research*, *111*(D6). https://doi.org/10.1029/2005JD005791

Chen, L., Gao, Y., Zhang, M., Fu, J. S., Zhu, J., Liao, H., et al. (2019). MICS-Asia III: Multi-model comparison and evaluation of aerosol over East Asia. *Atmospheric Chemistry and Physics*, *19*(18), 11911–11937. https://doi.org/10.5194/acp-19-11911-2019

Chen, Y., Street, J., & Paytan, A. (2006). Comparison between pure-water- and seawater-soluble nutrient concentrations of aerosols from the Gulf of Aqaba. *Marine Chemistry*, *101*(1–2), 141–152. https://doi.org/10.1016/j.marchem.2006.02.002

Chuang, P. Y., Duvall, R. M., Shafer, M. M., & Schauer, J. J. (2005). The origin of water soluble particulate iron in the Asian atmospheric outflow. *Geophysical Research Letters*, *32*(7). https://doi.org/10.1029/2004GL021946

Chueinta, W., Hopke, P. K., & Paatero, P. (2000). Investigation of sources of atmospheric aerosol at urban and suburban residential areas in Thailand by positive matrix factorization. *Atmospheric Environment*, *34*(20), 3319–3329. https://doi.org/10.1016/S1352-2310(99)00433-1

Clements, A. L., Fraser, M. P., Upadhyay, N., Herckes, P., Sundblom, M., Lantz, J., & Solomon, P. A. (2017). Source identification of coarse particles in the Desert Southwest, USA using positive matrix factorization. *Atmospheric Pollution Research*, *8*(5), 873–884. https://doi.org/10.1016/j.apr.2017.02.003

Cohen, D. D., Garton, D., Stelcer, E., Hawas, O., Wang, T., Poon, S., et al. (2004). Multielemental analysis and characterization of fine aerosols at several key ACE-Asia sites. *Journal of Geophysical Research*, *109*(D19). https://doi.org/10.1029/2003JD003569

da Silva, L. I. D., de Souza Sarkis, J. E., Zotin, F. M. Z., Carneiro, M. C., Neto, A. A., da Silva, A., et al. (2008). Traffic and catalytic converter – Related atmospheric contamination in the metropolitan region of the city of Rio de Janeiro, Brazil. *Chemosphere*, *71*(4), 677–684. https://doi.org/10.1016/j.chemosphere.2007.10.057

Dongarrà, G., Manno, E., Varrica, D., & Vultaggio, M. (2007). Mass levels, crustal component and trace elements in PM10 in Palermo, Italy. *Atmospheric Environment*, *41*(36), 7977–7986. https://doi.org/10.1016/j.atmosenv.2007.09.015

Fuzzi, S., Decesari, S., Facchini, M. C., Cavalli, F., Emblico, L., Mircea, M., et al. (2007). Overview of the inorganic and organic composition of size-segregated aerosol in Rondônia, Brazil, from the biomass-burning period to the onset of the wet season. *Journal of Geophysical Research*, *112*(D1). https://doi.org/10.1029/2005JD006741

Hamilton, D. S., Moore, J. K., Arneth, A., Bond, T. C., Carslaw, K. S., Hantson, S., et al. (2020). Impact of changes to the atmospheric soluble iron deposition flux on ocean biogeochemical cycles in the anthropocene. *Global Biogeochemical Cycles*, *34*(3), e2019GB006448. https://doi.org/10.1029/2019GB006448

Hamilton, D. S., Scanza, R. A., Feng, Y., Guinness, J., Kok, J. F., Li, L., et al. (2019). Improved methodologies for Earth system modelling of atmospheric soluble iron and observation comparisons using the Mechanism of Intermediate complexity for Modelling Iron (MIMI v1.0). *Geoscientific Model Development*, *12*(9), 3835–3862. https://doi.org/10.5194/gmd-12-3835-2019

Hand, J. L., Gill, T. E., & Schichtel, B. A. (2017). Spatial and seasonal variability in fine mineral dust and coarse aerosol mass at remote sites across the United States. *Journal of Geophysical Research: Atmospheres*, *122*(5), 3080–3097. https://doi.org/10.1002/2016JD026290

Hand, J. L., Schichtel, B. A., Pitchford, M., Malm, W. C., & Frank, N. H. (2012). Seasonal composition of remote and urban fine particulate matter in the United States. *Journal of Geophysical Research*, *117*(D5). https://doi.org/10.1029/2011JD017122

Harris, E., Sinha, B., Hoppe, P., Crowley, J. N., Ono, S., & Foley, S. (2012). Sulfur isotope fractionation during oxidation of sulfur dioxide: Gas-phase oxidation by OH radicals and aqueous oxidation by H_2O_2, O_3 and iron catalysis. *Atmospheric Chemistry and Physics*, *12*(1), 407–423. https://doi.org/10.5194/acp-12-407-2012

Hueglin, C., Gehrig, R., Baltensperger, U., Gysel, M., Monn, C., & Vonmont, H. (2005). Chemical characterisation of PM2.5, PM10 and coarse particles at urban, near-city and rural sites in Switzerland. *Atmospheric Environment*, *39*(4), 637–651. https://doi.org/10.1016/j.atmosenv.2004.10.027

Hurrell, J. W., Holland, M. M., Gent, P. R., Ghan, S., Kay, J. E., Kushner, P. J., et al. (2013). The Community Earth System Model: A framework for collaborative research. *Bulletin of the American Meteorological Society*, *94*(9), 1339–1360. https://doi.org/10.1175/BAMS-D-12-00121.1

Ito, A. (2015). Atmospheric processing of combustion aerosols as a source of bioavailable iron. *Environmental Science and Technology Letters*, *2*(3), 70–75. https://doi.org/10.1021/acs.estlett.5b00007

Ito, A., Lin, G., & Penner, J. E. (2018). Radiative forcing by light-absorbing aerosols of pyrogenetic iron oxides. *Scientific Reports*, *8*(1), 7347. https://doi.org/10.1038/s41598-018-25756-3

Ito, A., & Miyakawa, T. (2023). Aerosol iron from metal production as a secondary source of bioaccessible iron. *Environmental Science & Technology*, *57*(10), 4091–4100. https://doi.org/10.1021/acs.est.2c06472

Ito, A., Myriokefalitakis, S., Kanakidou, M., Mahowald, N. M., Scanza, R. A., Hamilton, D. S., et al. (2019). Pyrogenic iron: The missing link to high iron solubility in aerosols. *Science Advances*, *5*(5), eaau7671. https://doi.org/10.1126/sciadv.aau7671

Kim, E., Hopke, P. K., & Edgerton, E. S. (2003). Source identification of Atlanta aerosol by positive matrix factorization. *Journal of the Air & Waste Management Association*, *53*(6), 731–739. https://doi.org/10.1080/10473289.2003.10466209

Kok, J. F., Adebiyi, A. A., Albani, S., Balkanski, Y., Checa-Garcia, R., Chin, M., et al. (2021). Improved representation of the global dust cycle using observational constraints on dust properties and abundance. *Atmospheric Chemistry and Physics*, *21*(10), 8127–8167. https://doi.org/10.5194/acp-21-8127-2021

Kotronarou, A., & Sigg, L. (1993). Sulfur dioxide oxidation in atmospheric water: Role of iron(II) and effect of ligands. *Environmental Science & Technology*, *27*(13), 2725–2735. https://doi.org/10.1021/es00049a011

Kurisu, M., Sakata, K., Uematsu, M., Ito, A., & Takahashi, Y. (2021). Contribution of combustion Fe in marine aerosols over the northwestern Pacific estimated by Fe stable isotope ratios. *Atmospheric Chemistry and Physics*, *21*(20), 16027–16050. https://doi.org/10.5194/acp-21-16027-2021

Kyllönen, K., Vestenius, M., Anttila, P., Makkonen, U., Aurela, M., Wängberg, I., et al. (2020). Trends and source apportionment of atmospheric heavy metals at a subarctic site during 1996–2018. *Atmospheric Environment*, *236*, 117644. https://doi.org/10.1016/j.atmosenv.2020.117644

Lafon, S., Sokolik, I. N., Rajot, J. L., Caquineau, S., & Gaudichet, A. (2006). Characterization of iron oxides in mineral dust aerosols: Implications for light absorption. *Journal of Geophysical Research*, *111*(D21). https://doi.org/10.1029/2005JD007016

Laing, J. R., Hopke, P. K., Hopke, E. F., Husain, L., Dutkiewicz, V. A., Paatero, J., & Viisanen, Y. (2014). Long-term particle measurements in Finnish Arctic: Part II – Trend analysis and source location identification. *Atmospheric Environment*, *88*, 285–296. https://doi.org/10.1016/j.atmosenv.2014.01.015

Lamarque, J.-F., Bond, T. C., Eyring, V., Granier, C., Heil, A., Klimont, Z., et al. (2010). Historical (1850–2000) gridded anthropogenic and biomass burning emissions of reactive gases and aerosols: Methodology and application. *Atmospheric Chemistry and Physics*, *10*(15), 7017–7039. https://doi.org/10.5194/acp-10-7017-2010

Lee, Y. H., Lamarque, J.-F., Flanner, M. G., Jiao, C., Shindell, D. T., Berntsen, T., et al. (2013). Evaluation of preindustrial to present-day black carbon and its albedo forcing from Atmospheric Chemistry and Climate Model Intercomparison Project (ACCMIP). *Atmospheric Chemistry and Physics*, *13*(5), 2607–2634. https://doi.org/10.5194/acp-13-2607-2013

Liu, M., Matsui, H., Hamilton, D. S., Lamb, K. D., Rathod, S. D., Schwarz, J. P., & Mahowald, N. M. (2022). The underappreciated role of anthropogenic sources in atmospheric soluble iron flux to the Southern Ocean. *Npj Climate and Atmospheric Science*, *5*(1), 1–9. https://doi.org/10.1038/s41612-022-00250-w

Liu, X., Ma, P.-L., Wang, H., Tilmes, S., Singh, B., Easter, R. C., et al. (2016). Description and evaluation of a new four-mode version of the Modal Aerosol Module (MAM4) within version 5.3 of the Community Atmosphere Model. *Geoscientific Model Development*, *9*(2), 505–522. https://doi.org/10.5194/gmd-9-505-2016

Mackey, K. R. M., Hunter, D., Fischer, E. V., Jiang, Y., Allen, B., Chen, Y., et al. (2013). Aerosol-nutrient-induced picoplankton growth in Lake Tahoe. *Journal of Geophysical Research: Biogeosciences*, *118*(3), 1054–1067. https://doi.org/10.1002/jgrg.20084

Maenhaut, W., & Cafmeyer, J. (1998). Long-term atmospheric aerosol study at urban and rural sites in Belgium using multi-elemental analysis by particle-induced x-ray emission spectrometry and short-irradiation instrumental neutron activation analysis. *X-Ray Spectrometry*, *27*(4), 236–246. https://doi.org/10.1002/(SICI)1097-4539(199807/08)27:4<236::AID-XRS292>3.0.CO;2-F

Maenhaut, W., De Ridder, D. J. A., Fernández-Jiménez, M.-T., Hooper, M. A., Hooper, B., & Nurhayati, M. (2002). Long-term observations of regional aerosol composition at two sites in Indonesia. *Nuclear Instruments and Methods in Physics Research Section B: Beam Interactions with Materials and Atoms*, *189*(1), 259–265. https://doi.org/10.1016/S0168-583X(01)01054-0

Maenhaut, W., Fernández-Jiménez, M.-T., Rajta, I., & Artaxo, P. (2002). Two-year study of atmospheric aerosols in Alta Floresta, Brazil: Multielemental composition and source apportionment. *Nuclear Instruments and Methods in Physics Research Section B: Beam Interactions with Materials and Atoms*, *189*(1), 243–248. https://doi.org/10.1016/S0168-583X(01)01050-3

Maenhaut, W., Nava, S., Lucarelli, F., Wang, W., Chi, X., & Kulmala, M. (2011). Chemical composition, impact from biomass burning, and mass closure for PM2.5 and PM10 aerosols at Hyytiälä, Finland, in summer 2007. *X-Ray Spectrometry*, *40*(3), 168–171. https://doi.org/10.1002/xrs.1302

Maenhaut, W., Raes, N., Chi, X., Cafmeyer, J., Wang, W., & Salma, I. (2005). Chemical composition and mass closure for fine and coarse aerosols at a kerbside in Budapest, Hungary, in spring 2002. *X-Ray Spectrometry*, *34*(4), 290–296. https://doi.org/10.1002/xrs.820

Maenhaut, W., Salma, I., Cafmeyer, J., Annegarn, H. J., & Andreae, M. O. (1996). Regional atmospheric aerosol composition and sources in the eastern Transvaal, South Africa, and impact of biomass burning. *Journal of Geophysical Research*, *101*(D19), 23631–23650. https://doi.org/10.1029/95JD02930

Mahowald, N. M., Engelstaedter, S., Luo, C., Sealy, A., Artaxo, P., Benitez-Nelson, C., et al. (2009). Atmospheric iron deposition: Global distribution, variability, and human perturbations. *Annual Review of Marine Science*, *1*(1), 245–278. https://doi.org/10.1146/annurev.marine.010908.163727

Mahowald, N. M., Hamilton, D. S., Mackey, K. R. M., Moore, J. K., Baker, A. R., Scanza, R. A., & Zhang, Y. (2018). Aerosol trace metal leaching and impacts on marine microorganisms. *Nature Communications*, *9*(1), 2614. https://doi.org/10.1038/s41467-018-04970-7

Mahowald, N. M., Zender, C. S., Luo, C., Savoie, D., Torres, O., & del Corral, J. (2002). Understanding the 30-year Barbados desert dust record. *Journal of Geophysical Research*, *107*(D21), AAC7-1–AAC7-16. https://doi.org/10.1029/2002JD002097

Malm, W. C., Pitchford, M. L., McDade, C., & Ashbaugh, L. L. (2007). Coarse particle speciation at selected locations in the rural continental United States. *Atmospheric Environment*, *41*(10), 2225–2239. https://doi.org/10.1016/j.atmosenv.2006.10.077

Martin, J. H., Fitzwater, S. E., & Gordon, R. M. (1990). Iron deficiency limits phytoplankton growth in Antarctic waters. *Global Biogeochemical Cycles*, *4*(1), 5–12. https://doi.org/10.1029/GB004i001p00005

Martin, R. V., Jacob, D. J., Chance, K., Kurosu, T. P., Palmer, P. I., & Evans, M. J. (2003). Global inventory of nitrogen oxide emissions constrained by space-based observations of NO2 columns. *Journal of Geophysical Research*, *108*(D17). https://doi.org/10.1029/2003JD003453

Matsui, H., Mahowald, N. M., Moteki, N., Hamilton, D. S., Ohata, S., Yoshida, A., et al. (2018). Anthropogenic combustion iron as a complex climate forcer. *Nature Communications*, *9*(1), 1593. https://doi.org/10.1038/s41467-018-03997-0

McNeill, J., Snider, G., Weagle, C. L., Walsh, B., Bissonnette, P., Stone, E., et al. (2020). Large global variations in measured airborne metal concentrations driven by anthropogenic sources. *Scientific Reports*, *10*(1), 21817. https://doi.org/10.1038/s41598-020-78789-y

Menut, L., Forêt, G., & Bergametti, G. (2007). Sensitivity of mineral dust concentrations to the model size distribution accuracy. *Journal of Geophysical Research*, *112*(D10). https://doi.org/10.1029/2006JD007766

Miyakawa, T., Ito, A., Zhu, C., Shimizu, A., Matsumoto, E., Mizuno, Y., & Kanaya, Y. (2023). Trace elements in $PM_{2.5}$ aerosols in East Asian outflow in the spring of 2018: Emission, transport, and source apportionment. *Atmospheric Chemistry and Physics*, *23*(22), 14609–14626. https://doi.org/10.5194/acp-23-14609-2023

Mkoma, S. L., Maenhaut, W., Chi, X., Wang, W., & Raes, N. (2009). Characterisation of PM10 atmospheric aerosols for the wet season 2005 at two sites in East Africa. *Atmospheric Environment*, *43*(3), 631–639. https://doi.org/10.1016/j.atmosenv.2008.10.008

Mkoma, S. L., Wang, W., & Maenhaut, W. (2009). Seasonal variation of water-soluble inorganic species in the coarse and fine atmospheric aerosols at Dar es Salaam, Tanzania. *Nuclear Instruments and Methods in Physics Research Section B: Beam Interactions with Materials and Atoms*, *267*(17), 2897–2902. https://doi.org/10.1016/j.nimb.2009.06.099

Morera-Gómez, Y., Elustondo, D., Lasheras, E., Alonso-Hernández, C. M., & Santamaría, J. M. (2018). Chemical characterization of PM10 samples collected simultaneously at a rural and an urban site in the Caribbean coast: Local and long-range source apportionment. *Atmospheric Environment*, *192*, 182–192. https://doi.org/10.1016/j.atmosenv.2018.08.058

Moteki, N., Adachi, K., Ohata, S., Yoshida, A., Harigaya, T., Koike, M., & Kondo, Y. (2017). Anthropogenic iron oxide aerosols enhance atmospheric heating. *Nature Communications*, *8*(1), 15329. https://doi.org/10.1038/ncomms15329

Myriokefalitakis, S., Ito, A., Kanakidou, M., Nenes, A., Krol, M. C., Mahowald, N. M., et al. (2018). Reviews and syntheses: The GESAMP atmospheric iron deposition model intercomparison study. *Biogeosciences*, *15*(21), 6659–6684. https://doi.org/10.5194/bg-15-6659-2018

Ohata, S., Yoshida, A., Moteki, N., Adachi, K., Takahashi, Y., Kurisu, M., & Koike, M. (2018). Abundance of light-absorbing anthropogenic iron oxide aerosols in the urban atmosphere and their emission sources. *Journal of Geophysical Research: Atmospheres*, *123*(15), 8115–8134. https://doi.org/10.1029/2018JD028363

Okin, G. S., Baker, A. R., Tegen, I., Mahowald, N. M., Dentener, F. J., Duce, R. A., et al. (2011). Impacts of atmospheric nutrient deposition on marine productivity: Roles of nitrogen, phosphorus, and iron. *Global Biogeochemical Cycles*, *25*(2). https://doi.org/10.1029/2010GB003858

Paatero, P. (1997). Least squares formulation of robust non-negative factor analysis. *Chemometrics and Intelligent Laboratory Systems*, *37*(1), 23–35. https://doi.org/10.1016/S0169-7439(96)00044-5

Paatero, P., & Tapper, U. (1994). Positive matrix factorization: A non-negative factor model with optimal utilization of error estimates of data values. *Environmetrics*, *5*(2), 111–126. https://doi.org/10.1002/env.3170050203

Pinedo-González, P., Hawco, N. J., Bundy, R. M., Armbrust, E. V., Follows, M. J., Cael, B. B., et al. (2020). Anthropogenic Asian aerosols provide Fe to the North Pacific ocean. *Proceedings of the National Academy of Sciences*, *117*(45), 27862–27868. https://doi.org/10.1073/pnas.2010315117

Putaud, J.-P., Raes, F., Van Dingenen, R., Brüggemann, E., Facchini, M.-C., Decesari, S., et al. (2004). A European aerosol phenomenology—2: Chemical characteristics of particulate matter at kerbside, urban, rural and background sites in Europe. *Atmospheric Environment*, *38*(16), 2579–2595. https://doi.org/10.1016/j.atmosenv.2004.01.041

Putaud, J.-P., Van Dingenen, R., Alastuey, A., Bauer, H., Birmili, W., Cyrys, J., et al. (2010). A European aerosol phenomenology – 3: Physical and chemical characteristics of particulate matter from 60 rural, urban, and kerbside sites across Europe. *Atmospheric Environment*, *44*(10), 1308–1320. https://doi.org/10.1016/j.atmosenv.2009.12.011

Ramadan, Z., Song, X.-H., & Hopke, P. K. (2000). Identification of sources of Phoenix aerosol by positive matrix factorization. *Journal of the Air & Waste Management Association*, *50*(8), 1308–1320. https://doi.org/10.1080/10473289.2000.10464173

Rathod, S. (2023). Constraining present-day anthropogenic total iron emissions using model and observations. [Dataset]. *Zenodo*. https://doi.org/10.5281/zenodo.10069972

Rathod, S. D., Bond, T. C., Klimont, Z., Pierce, J. R., Mahowald, N., Roy, C., et al. (2022). Future $PM_{2.5}$ emissions from metal production to meet renewable energy demand. *Environmental Research Letters*, *17*(4), 044043. https://doi.org/10.1088/1748-9326/ac5d9c

Rathod, S. D., Hamilton, D. S., Li, L., Mahowald, N. M., Matsui, H., Pierce, J. R., & Bond, T. C. (2022). Atmospheric radiative and oceanic biological productivity responses to increasing anthropogenic combustion-iron emission in the 1850–2010 period. *Geophysical Research Letters*, *49*(16), e2022GL099323. https://doi.org/10.1029/2022GL099323

Rathod, S. D., Hamilton, D. S., Mahowald, N. M., Klimont, Z., Corbett, J. J., & Bond, T. C. (2020). A mineralogy-based anthropogenic combustion-iron emission inventory. *Journal of Geophysical Research: Atmospheres*, *125*(17), e2019JD032114. https://doi.org/10.1029/2019JD032114

Rienecker, M. M., Suarez, M. J., Gelaro, R., Todling, R., Bacmeister, J., Liu, E., et al. (2011). Merra: NASA's Modern-Era Retrospective analysis for research and applications. *Journal of Climate*, *24*(14), 3624–3648. https://doi.org/10.1175/JCLI-D-11-00015.1

Rodríguez, S., Alastuey, A., Alonso-Pérez, S., Querol, X., Cuevas, E., Abreu-Afonso, J., et al. (2011). Transport of desert dust mixed with North African industrial pollutants in the subtropical Saharan Air Layer. *Atmospheric Chemistry and Physics*, *11*(13), 6663–6685. https://doi.org/10.5194/acp-11-6663-2011

Rodríguez, S., Prospero, J. M., López-Darias, J., García-Alvarez, M.-I., Zuidema, P., Nava, S., et al. (2021). Tracking the changes of iron solubility and air pollutants traces as African dust transits the Atlantic in the Saharan dust outbreaks. *Atmospheric Environment*, *246*, 118092. https://doi.org/10.1016/j.atmosenv.2020.118092

Salma, I., Maenhaut, W., Annegarn, H. J., Andreae, M. O., Meixner, F. X., & Garstang, M. (1997). Combined application of INAA and PIXE for studying the regional aerosol composition in Southern Africa. *Journal of Radioanalytical and Nuclear Chemistry*, *216*(1), 143–148. https://doi.org/10.1007/BF02034512

Samset, B. H., Myhre, G., Herber, A., Kondo, Y., Li, S.-M., Moteki, N., et al. (2014). Modelled black carbon radiative forcing and atmospheric lifetime in AeroCom Phase II constrained by aircraft observations. *Atmospheric Chemistry and Physics*, *14*(22), 12465–12477. https://doi.org/10.5194/acp-14-12465-2014

Savoie, D. L., Prospero, J. M., Larsen, R. J., Huang, F., Izaguirre, M. A., Huang, T., et al. (1993). Nitrogen and sulfur species in Antarctic aerosols at Mawson, Palmer Station, and Marsh (King George Island). *Journal of Atmospheric Chemistry*, *17*(2), 95–122. https://doi.org/10.1007/BF00702821

Smichowski, P., Gómez, R., Dawidowski, L., Giné, M. F., Bellato, A. C. S., & Reich, L. (2004). Monitoring trace metals in urban aerosols from Buenos Aires city. Determination by plasma-based techniques. *Journal of Environmental Monitoring*, *6*(4), 286–294. https://doi.org/10.1039/B312446K

Smith, M. B., Mahowald, N. M., Albani, S., Perry, A., Losno, R., Qu, Z., et al. (2017). Sensitivity of the interannual variability of mineral aerosol simulations to meteorological forcing dataset. *Atmospheric Chemistry and Physics*, *17*(5), 3253–3278. https://doi.org/10.5194/acp-17-3253-2017

Solomon, P. A., Crumpler, D., Flanagan, J. B., Jayanty, R. K. M., Rickman, E. E., & McDade, C. E. (2014). U.S. National PM2.5 chemical speciation monitoring Networks—CSN and IMPROVE: Description of networks. *Journal of the Air & Waste Management Association*, *64*(12), 1410–1438. https://doi.org/10.1080/10962247.2014.956904

Streets, D. G., Bond, T. C., Carmichael, G. R., Fernandes, S. D., Fu, Q., He, D., et al. (2003). An inventory of gaseous and primary aerosol emissions in Asia in the year 2000. *Journal of Geophysical Research*, *108*(D21). https://doi.org/10.1029/2002JD003093

Tsigaridis, K., Daskalakis, N., Kanakidou, M., Adams, P. J., Artaxo, P., Bahadur, R., et al. (2014). The AeroCom evaluation and intercomparison of organic aerosol in global models. *Atmospheric Chemistry and Physics*, *14*(19), 10845–10895. https://doi.org/10.5194/acp-14-10845-2014

Ulbrich, I. M., Canagaratna, M. R., Zhang, Q., Worsnop, D. R., & Jimenez, J. L. (2009). Interpretation of organic components from positive matrix factorization of aerosol mass spectrometric data. *Atmospheric Chemistry and Physics*, *9*(9), 2891–2918. https://doi.org/10.5194/acp-9-2891-2009

van der Werf, G. R., Randerson, J. T., Giglio, L., van Leeuwen, T. T., Chen, Y., Rogers, B. M., et al. (2017). Global fire emissions estimates during 1997–2016. *Earth System Science Data*, *9*(2), 697–720. https://doi.org/10.5194/essd-9-697-2017

Van Dingenen, R., Raes, F., Putaud, J.-P., Baltensperger, U., Charron, A., Facchini, M.-C., et al. (2004). A European aerosol phenomenology—1: Physical characteristics of particulate matter at kerbside, urban, rural and background sites in Europe. *Atmospheric Environment*, *38*(16), 2561–2577. https://doi.org/10.1016/j.atmosenv.2004.01.040

Vecchi, R., Chiari, M., D'Alessandro, A., Fermo, P., Lucarelli, F., Mazzei, F., et al. (2008). A mass closure and PMF source apportionment study on the sub-micron sized aerosol fraction at urban sites in Italy. *Atmospheric Environment*, *42*(9), 2240–2253. https://doi.org/10.1016/j.atmosenv.2007.11.039

Virkkula, A., Aurela, M., Hillamo, R., Mäkelä, T., Pakkanen, T., Kerminen, V.-M., et al. (1999). Chemical composition of atmospheric aerosol in the European subarctic: Contribution of the Kola Peninsula smelter areas, central Europe, and the Arctic Ocean. *Journal of Geophysical Research*, *104*(D19), 23681–23696. https://doi.org/10.1029/1999JD900426

Wang, R., Balkanski, Y., Boucher, O., Bopp, L., Chappell, A., Ciais, P., et al. (2015). Sources, transport and deposition of iron in the global atmosphere. *Atmospheric Chemistry and Physics*, *15*(11), 6247–6270. https://doi.org/10.5194/acp-15-6247-2015

Wang, Y., Puthussery, J. V., Yu, H., & Verma, V. (2020). Synergistic and antagonistic interactions among organic and metallic components of the ambient particulate matter (PM) for the cytotoxicity measured by Chinese hamster ovary cells. *Science of the Total Environment*, *736*, 139511. https://doi.org/10.1016/j.scitotenv.2020.139511

Yin, J., Cumberland, S. A., Harrison, R. M., Allan, J., Young, D. E., Williams, P. I., & Coe, H. (2015). Receptor modelling of fine particles in southern England using CMB including comparison with AMS-PMF factors. *Atmospheric Chemistry and Physics*, *15*(4), 2139–2158. https://doi.org/10.5194/acp-15-2139-2015

Yoshida, A., Moteki, N., Ohata, S., Mori, T., Koike, M., Kondo, Y., et al. (2020). Abundances and microphysical properties of light-absorbing iron oxide and black carbon aerosols over East Asia and the Arctic. *Journal of Geophysical Research: Atmospheres*, *125*(15), e2019JD032301. https://doi.org/10.1029/2019JD032301

Yoshida, A., Ohata, S., Moteki, N., Adachi, K., Mori, T., Koike, M., & Takami, A. (2018). Abundance and emission flux of the anthropogenic iron oxide aerosols from the East Asian continental outflow. *Journal of Geophysical Research: Atmospheres*, *123*(19), 11194–11209. https://doi.org/10.1029/2018JD028665

Yuan, Z. B., Yu, J. Z., Lau, A. K. H., Louie, P. K. K., & Fung, J. C. H. (2006). Application of positive matrix factorization in estimating aerosol secondary organic carbon in Hong Kong and its relationship with secondary sulfate. *Atmospheric Chemistry and Physics*, *6*(1), 25–34. https://doi.org/10.5194/acp-6-25-2006

Zhu, L., Henze, D. K., Cady-Pereira, K. E., Shephard, M. W., Luo, M., Pinder, R. W., et al. (2013). Constraining U.S. ammonia emissions using TES remote sensing observations and the GEOS-Chem adjoint model. *Journal of Geophysical Research: Atmospheres*, *118*(8), 3355–3368. https://doi.org/10.1002/jgrd.50166

References From the Supporting Information

Corral, A. F., Dadashazar, H., Stahl, C., Edwards, E.-L., Zuidema, P., & Sorooshian, A. (2020). Source apportionment of aerosol at a coastal site and relationships with precipitation chemistry: A case study over the Southeast United States. *Atmosphere*, *11*(11), 1212. https://doi.org/10.3390/atmos11111212

Das, R., Wang, X., Itoh, M., Shiodera, S., & Kuwata, M. (2019). Estimation of metal emissions from tropical peatland burning in Indonesia by controlled laboratory experiments. *Journal of Geophysical Research: Atmospheres*, *124*(12), 6583–6599. https://doi.org/10.1029/2019JD030364

Hyslop, N. P., & White, W. H. (2009). Estimating precision using duplicate measurements. *Journal of the Air & Waste Management Association*, *59*(9), 1032–1039. https://doi.org/10.3155/1047-3289.59.9.1032

Schroth, A. W., Crusius, J., Sholkovitz, E. R., & Bostick, B. C. (2009). Iron solubility driven by speciation in dust sources to the ocean. *Nature Geoscience*, *2*(5), 337–340. https://doi.org/10.1038/ngeo501

Sholkovitz, E. R., Sedwick, P. N., & Church, T. M. (2009). Influence of anthropogenic combustion emissions on the deposition of soluble aerosol iron to the ocean: Empirical estimates for island sites in the North Atlantic. *Geochimica et Cosmochimica Acta*, *73*(14), 3981–4003. https://doi.org/10.1016/j.gca.2009.04.029